Tectonophysics 690 (2016) 76–96

Contents lists available at ScienceDirect

Tectonophysics

journal homepage: www.elsevier.com/locate/tecto

Crestal fault geometries reveal late halokinesis and collapse of the Samson Dome, Northern Norway: Implications for petroleum systems in the Barents Sea

Nathalia H. Mattos [a,*], Tiago M. Alves [a], Kamaldeen O. Omosanya [b]

[a] 3D Seismic Lab, School of Earth and Ocean Sciences, Cardiff University, Main Building-Park Place, CF10 3AT Cardiff, United Kingdom
[b] Department of Petroleum Engineering and Applied Geophysics, Norwegian University of Science and Technology, 7491, Trondheim, Norway

ARTICLE INFO

Article history:
Received 7 September 2015
Received in revised form 11 April 2016
Accepted 30 April 2016
Available online 3 May 2016

Keywords:
Barents Sea
Samson Dome
Halokinesis
Salt collapse
Tectonic stress
Fluid-flow

ABSTRACT

This paper uses 2D and high-quality 3D seismic reflection data to assess the geometry and kinematics of the Samson Dome, offshore Norway, revising the implications of the new data to hydrocarbon exploration in the Barents Sea. The study area was divided into three (3) zones in terms of fault geometries and predominant strikes. Displacement-length (D-x) and Throw-depth (T-z) plots showed faults to consist of several segments that were later dip-linked. Interpreted faults were categorised into three families, with Type A comprising crestal faults, Type B representing large E-W faults, and Type C consisting of polygonal faults. The Samson Dome was formed in three major stages: a) a first stage recording buckling of the post-salt overburden and generation of radial faults; b) a second stage involving dissolution and collapse of the dome, causing subsidence of the overburden and linkage of initially isolated fault segments; and c) a final stage in which large fault segments were developed. Late Cretaceous faults strike predominantly to the NW, whereas NE-trending faults comprise Triassic structures that were reactivated in a later stage. Our work provides scarce evidence for the escape of hydrocarbons in the Samson Dome. In addition, fault analyses based on present-day stress distributions indicate a tendency for 'locking' of faults at depth, with the largest leakage factors occurring close to the surface. The Samson Dome is an analogue to salt structures in the Barents Sea where oil and gas exploration has occurred with varied degrees of success.

1. Introduction

Faults and fractures constitute evidence for tectonic movements during crustal deformation, being important in the entrapment and migration of fluids (Aydin, 2000; Biddle, 1985; Childs et al., 1997; Knipe, 1997; Knipe et al., 1998; Smith et al., 1990; Walsh et al., 1998). In such a context, deformation during regional extensional or shortening events is favoured in sedimentary basins with thick evaporite accumulations, as compared to basins lacking salt (Hudec and Jackson, 2007; Vendeville and Jackson, 1992; Vendeville, 2002; Stewart, 2006). Halokinesis can lead to the development of complex families of faults, which will form structural compartments, or act as fluid pathways in reservoir and seal units (Alves et al., 2009; Carruthers et al., 2013; Gamboa et al., 2010; Stewart, 2006; Talbot et al., 1991). These fault-bounded compartments have a crucial impact on the volume of trapped subsurface hydrocarbons and, if not assessed in the early stages of the reservoir evaluation, may result in the early abandonment of otherwise viable fields (Caine et al., 1996; Jolley et al., 2010; Knipe, 1997; Knipe et al., 1998).

The Barents Sea is a region where hydrocarbon potential is larger in basins associated with salt tectonics (Bugge et al., 2002; Chand et al., 2008; Henriksen et al., 2011a,b; Koyi et al., 1993; Nilsen et al., 1995; Perez-Garcia et al., 2013; Stoupakova et al., 2011). However, halokinetic structures in the region are poorly studied due to the sparse availability of high-resolution data. So far, most published studies on the Barents Sea used 2D seismic data of regional extent and limited resolution (Breivik et al., 1995, 1998; Faleide et al., 1993; Gabrielsen et al., 1990; Gabrielsen, 1984; Gernigon and Brönner, 2012; Glørstad-Clark et al., 2010; Gudlaugsson et al., 1998). This relative absence of high-quality 3D seismic data has led to incomplete structural interpretations in areas where salt tectonics is an important control on Late Palaeozoic and Early Mesozoic reservoir compartmentalisation, as shown in this paper.

The present study is focused on the Samson Dome (Fig. 1), a structural high located in the Ottar Basin (Breivik et al., 1995). The Ottar Basin comprises itself a Permian depocentre developed on the Bjarmeland Platform (Gabrielsen et al., 1990). The anticlinal structure that forms the Samson Dome is thought to result from the Middle to Late Triassic halokinesis (Breivik et al., 1995, 1998; Gabrielsen et al., 1990). Furthermore, Vadakkepuliyambatta et al. (2013) found shallow gas and widespread evidence for fluid leakage through faults in the

* Corresponding author.
E-mail address: mattosnh@cardiff.ac.uk (N.H. Mattos).

http://dx.doi.org/10.1016/j.tecto.2016.04.043

Samson Dome. This leakage zone, with approximately 141 km^2, was considered as one of the largest fluid-flow features in the western Barents Sea (Vadakkepuliyambatta et al., 2013).

This paper uses 3D and 2D seismic data to reassess the geometry and kinematics of the Samson Dome, Barents Sea, and includes an evaluation of the timing of salt growth, collapse and associated fault formation. In summary, this work aims to address the following questions:

a) What is the history of fault growth and propagation in the Samson Dome area, and how does halokinesis influence fault styles?

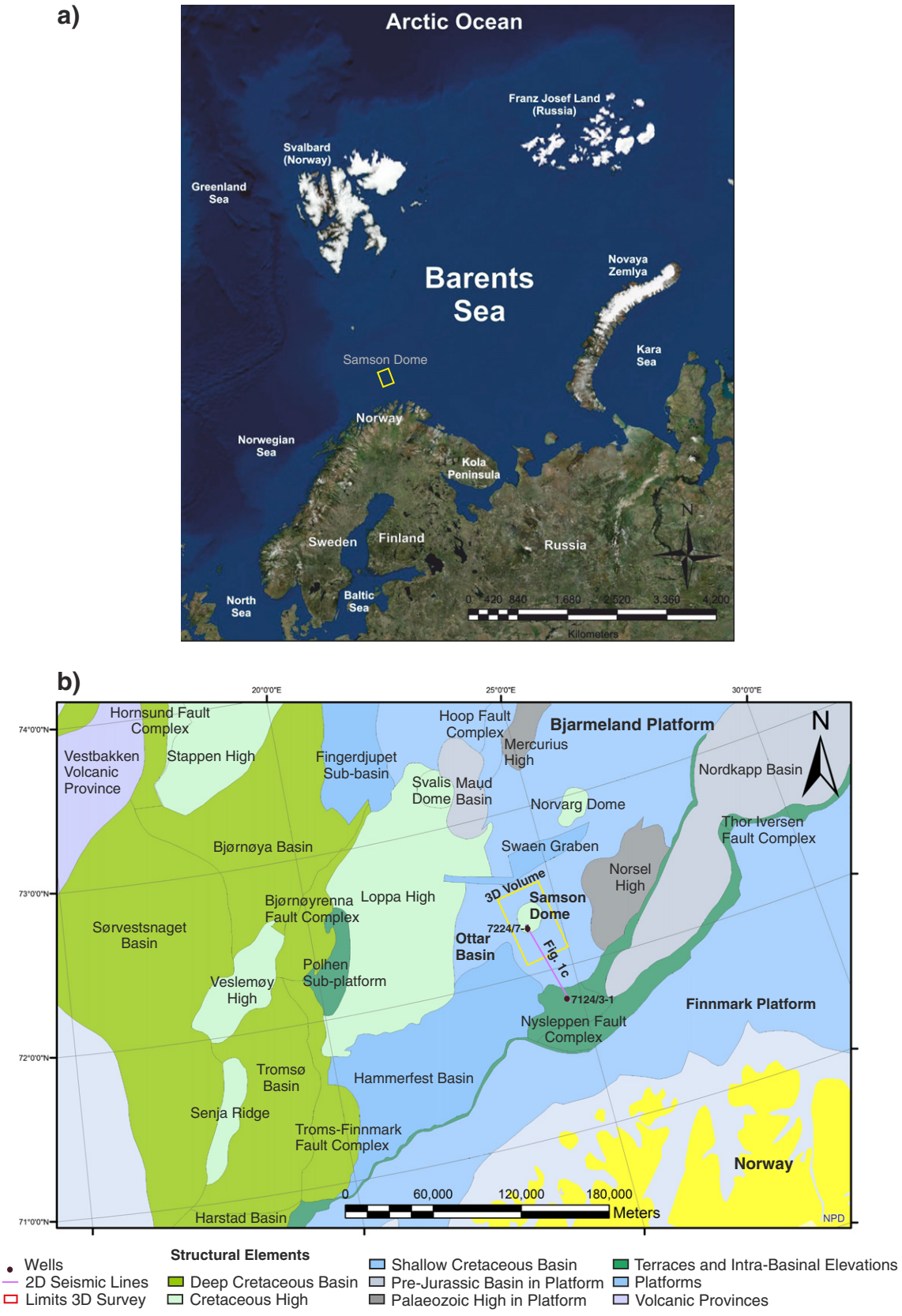

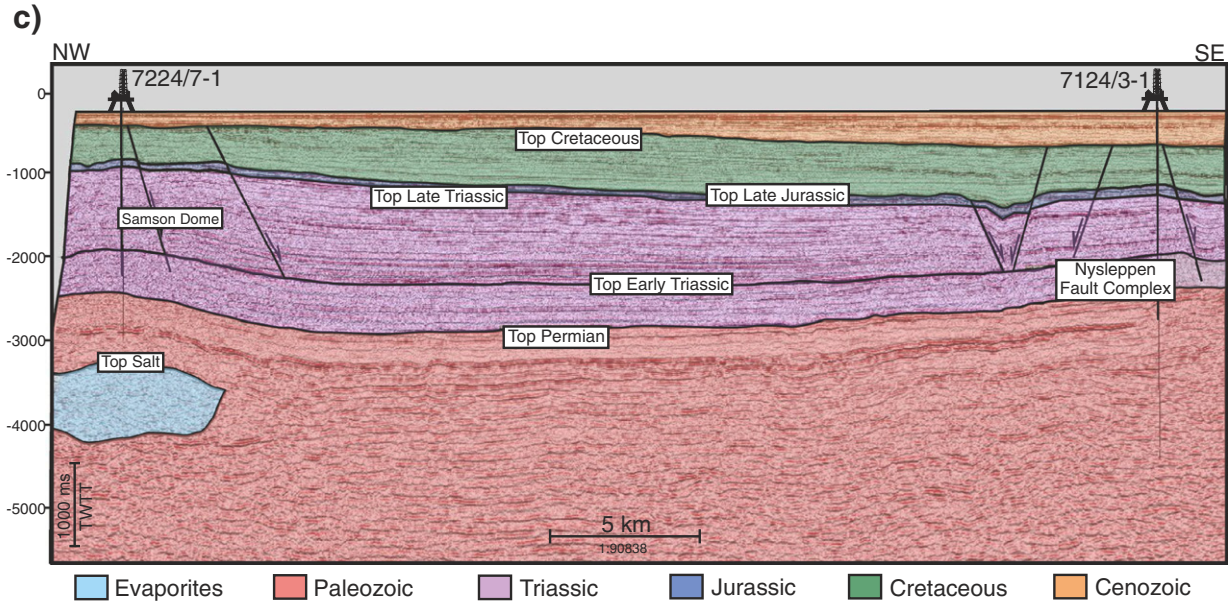

Fig. 1. a) Location map of the Barents Sea and its main structural boundaries. The Barents Sea is limited to the west by the Norwegian Sea, to the north by the Svalbard Archipelago (Norway) and Franz Josef Land (Russia), to the east by the Novaya Zemlya and to the south by the Norwegian Mainland and the Kola Peninsula. b) Detailed map of the Barents Sea highlighting main structures at a regional scale. The location of the 3D seismic cube and 2D seismic line used in this work are shown on the map. c) Interpreted regional seismic section of the Bjarmeland platform, indicating the location of the Samson Dome and Nyslepp Fault Complex. Wells 7224/7-1 and 7214/3-1 are located along this seismic profile. The map in b) was modified after the Norwegian Petroleum Directorate FactMaps (2015).

b) Is there late strike-slip reactivation affecting the Samson Dome during the Late Mesozoic?

c) How does the current stress regime of the Barents Sea control fluid flow and trapping in the study area?

d) How can the Samson Dome provide insights into the Mesozoic–Cenozoic evolution of the Barents Sea, contributing to the analysis of seal unit competence and fluid migration in regions with similar halokinetic structures?

This study is the first to test previously published 2D structural models for the Samson Dome by using a 3D seismic dataset. Stratigraphic and structural features are enhanced in the interpreted 3D seismic volume, allowing a more detailed evaluation of the dome as a potential fluid-flow and seepage zone. The new data not only provide an insight into the Mesozoic–Cenozoic evolution of the Barents Sea, but also contributes to the analysis of seal unit competence and timings of fluid migration in areas with similar halokinetic structures.

2. Geological setting

The Barents Sea is an epicontinental sea located in northernmost Europe, with an area of ~1.3 million km^2 and an average water depth of 300 m (Doré, 1995). The northern limits of the Barents Sea are the Svalbard Archipelago and Franz Josef Land, and its eastern boundary is Novaya Zemlya (Fig. 1a). To the south, the Barents Sea is bounded by the Norwegian Mainland and the Kola Peninsula (Barrère et al., 2009; Doré, 1995; Faleide et al., 1984, 1993; Henriksen et al., 2011a; Vorren et al., 1991) (Fig. 1a).

The Barents Sea comprises several platforms, structural highs, and basins, formed at different stages during the Late Palaeozoic and Mesozoic (Doré, 1991; Gabrielsen, 1984; Nøttvedt et al., 1993; Ritzmann and Faleide, 2007). One of these basins, the Ottar Basin, comprises a 170 km-long and 50–80 km-wide depocentre developed during Late Devonian–Middle Carboniferous rifting (Breivik et al., 1995; Gudlaugsson et al., 1998; Dengo and Røssland, 2013; Jensen and Sørensen, 1992). The Ottar Basin is bounded by the Norsel High to the east and by the Hammerfest Basin to the southwest (Fig. 1b). Its northwest limit coincides with the Loppa High, the Maud Basin, and the Mercurius High, whereas the Ottar Basin is bounded by the Nordkapp Basin to the northeast (Fig. 1b). The Ottar Basin comprises the Swaen Graben and two salt structures, the Norvarg and Samson Domes (Gudlaugsson et al., 1998).

In map view, the Samson Dome has been described as having an elliptic to circular geometry, with a diameter of ~18 km. It exhibits a radial fault pattern generated due to the extension of post-salt Mesozoic sequences (Gabrielsen et al., 1990), and was later reactivated during the Late Cretaceous and Early Tertiary (Breivik et al., 1995). Data in Breivik et al. (1995) and Gabrielsen et al. (1990) show a lenticular evaporite body at depth, with a maximum thickness of 3.5 km and an estimated volume of 500–600 km^3 (Fig. 2). Breivik et al. (1995) suggested that the primary reason for the very moderate salt movement in the Samson Dome was the presence of thick and competent overburden rocks (i.e., Lower Permian carbonates and Upper Permian silicified strata) above Upper Palaeozoic evaporites.

2.1. Palaeozoic tectono-stratigraphic setting of the western Barents Sea

The Caledonian Orogeny deformed the crystalline basement of the Barents Sea from the Late Silurian to Early Devonian (Faleide et al., 1984; Gernigon and Brönner, 2012; Gudlaugsson et al., 1998). Compression during the Caledonian Orogeny was followed by rifting in the Mesozoic, and continental breakup of the Northern Atlantic margins in Norway and Greenland during the Cenozoic (Faleide et al., 2008; Gabrielsen et al., 1990; Gee et al., 2008; Gernigon et al., 2014; Glørstad-Clark et al., 2010). The Caledonian Orogeny played a significant role in influencing the location and orientation of sedimentary basins in the Barents Sea (Breivik et al., 2002; Faleide et al., 1993; Gernigon and Brönner, 2012; Gudlaugsson et al., 1998; Ritzmann and Faleide, 2007; Worsley, 2008). Extension, rifting and plate separation marked the early stages of the Caledonide Orogen in Scandinavia during the breakup of Rodinia in the Neoproterozoic (Cocks and Torsvik, 2005; Soper et al., 1992; Torsvik et al., 1996).

The Caledonide Orogen resulted in the subduction of the Iapetus Ocean margins during the Late Cambrian-Early Ordovician (Finnmarkian event; Roberts, 2003). Orogenesis continued during the Early Ordovician, and recorded the obduction of ophiolites in Central Norway (Trondheim event). The Taconian event, dated as Middle to Late Ordovician, marked the beginning of anticlockwise rotation of

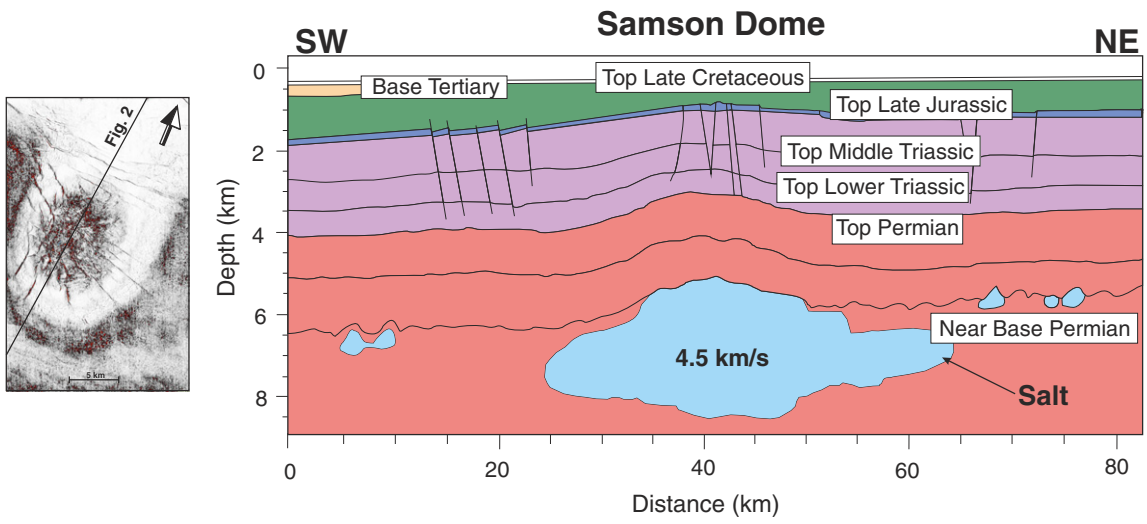

Fig. 2. Interpretation of a SW–NE seismic line across the Samson Dome showing the bottom depth of this salt anticline at a depth of ~8.5 km. This salt structure has been interpreted as a salt body with a maximum thickness of 3.5 km and an estimated volume of 500–600 km3. The estimated p-wave velocity of the salt body is ~4.5 km/s. Figure modified from Breivik et al. (1995).

Baltica away from Siberia. This was followed by the Scandian event, which witnessed the closure of the Iapetus Ocean in the Middle Silurian to Early Devonian (Faleide et al., 1984; Gee et al., 2008; Gudlaugsson et al., 1998; Ritzmann and Faleide, 2007; Roberts, 2003; Soper et al., 1992).

From Early to Middle Devonian, gravitational collapse of the Caledonian Mountains Chain resulted in widespread extension in the western Barents Sea (Faleide et al., 1996; Roberts, 2003; Worsley, 2008). Despite the lack of information regarding the development of sedimentary basins at this stage (Gabrielsen et al., 1990; Gudlaugsson et al., 1998), the western Barents Sea suggestively acted as a transfer zone linking Norway and Greenland during this first episode of Atlantic rifting (Doré, 1991; Gudlaugsson et al., 1998).

From Late Devonian to Middle Carboniferous, the western Barents Sea recorded multiple episodes of extension, a character leading to the development of a complex system of rift basins limited by structural highs (Dengo and Røssland, 2013; Faleide et al., 1984; Gabrielsen et al., 1990; Nøttvedt et al., 1993). In particular, Middle Carboniferous rifting was accompanied by important strike-slip tectonics, and several NE-trending basins were developed above NE-trending horsts and grabens that followed the structural fabric of the Caledonian basement (Gudlaugsson et al., 1998; Worsley, 2008). Large-scale basins, such as the Nordkapp, Bjørnøya, Tromsø, Hammerfest, Maud and Ottar Basins, were generated at this time (Fig. 1) (Dengo and Røssland, 2013; Faleide et al., 1993; Gabrielsen et al., 1990; Gudlaugsson et al., 1998).

An expansion in the sea area occurred in the Late Carboniferous, but tectonic activity diminished soon after until the Early Permian. In such a setting, the deposition of evaporites marks the end of rifting and the beginning of thermal subsidence in the region (Dengo and Røssland, 2013). As the Barents Sea moved further north during the Middle Permian, within a semi-arid climatic belt, it favoured the development of a post-rift carbonate platform dominated by warm-water limestones and evaporites (Elvebakk et al., 2002; Faleide et al., 1984; Gudlaugsson et al., 1998; Johansen et al., 1993; Stemmerik, 2000). The closure of the Uralian Sea during the Late Permian, however, affected the entire Barents Shelf by increasing subsidence rates and changing depositional stacking patterns from carbonates and evaporites to clastic, organoclastic and cherty sediments (Alves, 2016; Johansen et al., 1993; Worsley, 2008). Late Permian subsidence, together with the influence of extensional events in the western Barents Sea, resulted in the full establishment of the area currently denoted as the Bjarmeland Platform (Breivik et al., 1995).

2.2. Mesozoic–Cenozoic evolution of the western Barents Sea

During the Mesozoic, the Barents Sea was affected on its northern and western borders by the break-up of the Laurasian supercontinent, with subsequent opening of the Eurasian Basin and Norwegian-Greenland Sea (Faleide et al., 1993). The climate became humid, resulting in the deposition of large amounts of non-marine, nearshore and shallow-marine sediments derived from the Uralian Orogen (Glørstad-Clark et al., 2010; Johansen et al., 1993; Smelror et al., 2009). Strata in the western Barents Sea were, at this time, deposited during successive episodes of transgression and regression in sea level.

Tectonic activity in the western Barents Sea was relatively moderate during the Triassic, and the region became a shallow-water siliciclastic shelf at this time (Klausen and Mørk, 2014; Klausen et al., 2015; Mørk and Elvebakk, 1999). The first salt movements in the Ottar Basin took place from Middle Triassic to Late Triassic, resulting from gravitational instability generated by: a) loading gradients imposed by an NW-prograding shelf, and b) the reactivation of basement faults (Breivik et al., 1995). Passive margin subsidence, active faulting along the western margin of the Barents Sea (including the Bjarmeland Platform), and variations in the sedimentary supply affected the relationship between sedimentary infill and accommodation space during the Triassic (Gabrielsen et al., 1990; Glørstad-Clark et al., 2010; Klausen et al., 2015; Smelror et al., 2009). The Middle Triassic in the western Barents Sea was characterised by a central marine shelf where organic-rich mudstone accumulated in restricted anoxic conditions (Smelror et al., 2009). In the Late Triassic, another extensional event took place in the Barents Sea, resulting in the formation of an extensive coastal plain (Faleide et al., 1984; Glørstad-Clark et al., 2010; Smelror et al., 2009; Klausen and Mørk, 2014).

The Jurassic was marked by a major rifting episode. Early Jurassic deposition in the Ottar Basin started with sandstones and subordinated shales (Tubåen Formation) in a high-energy (transitional) marine setting (Dalland et al., 1988; Smelror, 1994). Depositional environments evolved from tidal flats to floodplains in the Pliensbachian, as indicated by the deposition of interbedded siltstones, sandstones, shales and claystones in the Nordmela Formation. During the Middle Jurassic, the Atlantic rifting affected the entire North Atlantic, opening a large marine gateway from the North Sea (and further south) to the study area. This event is recorded by the deposition of well-sorted and mineralogically mature sandstones in the Stø Formation (Faleide et al., 2008). The

Middle and Late Jurassic were dominated by regional extension and development of relatively minor strike-slip fault systems. Block faulting occurred in the Middle Jurassic and increased during the Late Jurassic and Early Cretaceous, culminating in the formation of large basins bounded by salt structures and major structural highs (Gabrielsen et al., 1990).

The Cretaceous started with intense rifting and subsidence in the western Barents Sea, whereas its eastern part remained quite stable (Faleide et al., 1993). Rifting resulted in the decoupling of the Harstad, Tromsø and Bjørnøya basins from the remainder of the Barents Sea (Smelror et al., 2009). In the Late Cretaceous, rifting in the North Atlantic led to the reactivation of normal faults on the western margin, together with local compression and uplift on the Svalbard Platform (Faleide et al., 1984, 1993; Gabrielsen et al., 1990). Tectonic subsidence, however, continued in other parts of the Barents Sea. The sedimentary infill came both from the eastern and the northern Barents Sea, which were uplifted at this time (Johansen et al., 1993; Smelror et al., 2009).

At the Cretaceous-Paleogene boundary, extension between Norway and Greenland was replaced by strike-slip deformation, resulting in the formation of the Sørvestsnaget Basin (Breivik et al., 1998; Ryseth et al., 2003). The final stage of lithospheric breakup between Norway and Greenland occurred at the Paleocene–Eocene boundary, with subsequent opening of the Norwegian-Greenland Sea at 55–54 Ma (Faleide et al., 2008). The opening of the Norwegian-Greenland Sea resulted in the salt diapirism through normal faults in the Sørvestsnaget Basin (Perez-Garcia et al., 2013). During the Eocene, deep-marine conditions predominated in the western Barents Sea, as recorded by the deposition of sands from submarine fans (Safronova et al., 2014). From the Middle Miocene to the present day, the Barents Sea was uplifted in its eastern part (Dengo and Røssland, 2013). This uplift is also associated with glacial erosion of the Barents Shelf during the Plio-Pleistocene (Faleide et al., 2008).

2.3. In-situ stress conditions in the Barents Sea

At present, regional data record well-defined maximum strike-slip to compressive NW-trending stresses in the central and the western parts of the European Plate. The average azimuth of these stresses approaches 140° (Gölke and Coblentz, 1996; Klein and Barr, 1986; Müller et al., 1992). Exceptions to this regional stress distribution are found in Scandinavia (Bungum et al., 1991; Müller et al., 1992; Ranalli and Chandler, 1975; Stephansson, 1993). Earthquake focal mechanisms and borehole data from the Finnmark Platform indicate compressional stress regimes at shallow depths, with reverse faults responding to a maximum horizontal stress σ_H trending either N–S or E–W (Fig. 3).

The existence of focal mechanisms for only five (5) earthquakes, the small seismological coverage and the low number of stress measurements makes it difficult to draw any conclusion about the general stress orientation and the tectonic regime in the broader Barents Sea (Brudy and Kjørholt, 2001; Lindholm et al., 1995, 2000). Nevertheless, the analysis of borehole breakouts (Fejerskov et al., 2000; Gölke and Brudy, 1996), regional earthquake focal mechanisms (Lindholm et al., 2000) and borehole measurements (Fejerskov et al., 2000) for the broader western Barents Sea indicate a N–S maximum horizontal stress direction and a mean σ_H azimuth of N177.24° ± 46.91°E (Fig. 3). The broad standard deviation for the average σ_H azimuth results from the large scatter of stress data obtained for the region. In-situ stress data indicate a clockwise rotation of the azimuth from WNW–ESE in the North Sea, to NW–SW in the Norwegian Sea and N–S in the Barents Sea (Fig. 3). This azimuth rotation suggests ridge push to be the principal stress-generating mechanism in the western Barents Sea (Lindholm et al., 2000). Another possible explanation for the different stress azimuths recorded in Finnmark and Barents Sea, compared to the general NW–SE trend for Europe, relates to the superposition of local stress sources on regional stress fields (Gölke and Brudy, 1996). Sources of local stress include the influence of local structures such as salt anticlines, salt diapirs, faults and folds, and lateral variations in subsurface rock properties (Brudy and Kjørholt, 2001; Fejerskov et al., 2000).

3. Data and methods

The interpreted 3D seismic volume covers an area of 1840 km^2 on the Bjarmeland Platform, at a maximum water depth of approximately 296 m (Fig. 1). The interpreted seismic data are pre-stack time migrated with a 12.5 × 25 m line spacing, and were acquired with a 10 × 6000 m array of streamers, each with 480 geophones. The seismic data are in the time domain, zero-phased, and were processed within a 4 ms vertical sampling window. The seismic sections are displayed in normal SEG convention for a zero-phase wavelet such that an increase in acoustic impedance with depth is a peak or positive reflection. Peaks are black reflections on seismic sections and relative decreases in acoustic impedance with depth are shown as negative or red seismic reflections (Figs. 4, 5 and 6).

Data processing included resampling, TAU-P linear noise attenuation, TAU-P domain deconvolution and zero-phase conversions undertaken prior to the 120-fold stacking of seismic traces. Three-dimensional pre-stack time migration used the Kirchhoff algorithm. In addition to 3D seismic data, the regional 2D seismic line SG8737-112 was used to tie the observed structures to the geological context of the Bjarmeland Platform and surrounding areas (Fig. 1a and b). Wells 7224/7-1 and 7214/3-1 are located along the interpreted 2D seismic line in Fig. 1c.

Well 7224/7-1 crossed the Samson Dome as a wildcat drilled by Den Norske Stats Oljeselskap A.S. in 1988. Well 7224/7-1 aimed at evaluating the reservoir potential of Late Triassic and Early Jurassic sandstones, and tested previous geophysical and structural interpretations. The well has a total depth of 3067 m (RKB) and penetrates strata from the Sassendalen Group (Early to Middle Triassic) to the Nordland Group (Pleistocene-Pliocene) (Fig. 4).

Well 7124/3-1 was a wildcat drilled by Saga Petroleum ASA in 1987. This well penetrated the Nyslepp Fault Complex, east of the Hammerfest Basin, and reached a total depth of 4730 m. Its primary goals were to test hydrocarbons from Middle Jurassic, to investigate the source rock potential of Triassic rocks, and to characterise Upper Carboniferous reservoir rocks. Well 7124/3-1 is the reference well for the Bjarmeland Group and Ørret Formation (Late Carboniferous-Early Permian). Strata penetrated by this well range from the Late Carboniferous (Ørn Formation) to the Pleistocene-Pliocene (Nordland Group) (Fig. 1c).

Seismic interpretation included horizon and fault mapping, seismic attributes and time-depth conversions on Petrel®. For time-depth conversions, we used an average p-wave velocity of 5500 m/s TWT observed in strata crossed by well 7224/7-1. As the well 7224/7-1 was drilled without crossing the Permian strata, we used p-wave velocities of 5800 m/s for Upper Permian strata and 6000 m/s for the Mid Permian, based on the average velocities on well 7124/3-1 (Alves, 2016). These velocities were used to convert mapped faults and horizons to depth and to obtain the true dip values of faults.

Eight (8) key seismic reflections, including the seafloor (Figs. 4, 5 and 6), were mapped every 10 lines (125 m) once well 7224/7-1 was tied to the seismic data. Smaller line intervals of 2–5 lines (25 to 62.5 m) were used to map the Samson Dome as a discrete structure. Based on the internal character and the geometry of the interpreted seismic reflections and on the correlation of these horizons with the formation tops of well 7224/7-1 (Larssen et al., 2002), the study area was divided into five stratigraphic units ranging from the Late Palaeozoic (Unit 1) to the Cenozoic (Unit 5) (Fig. 4). The interpreted stratigraphic markers include Middle Permian (H_1), Late Permian (H_2), Early Triassic (H_3), Middle Triassic (horizons H_4 and H_5), Late Triassic (H_6) and Late Cretaceous (H_7) unconformities (Figs. 5 and 6). Structural maps of horizons H_1 and H_5 complemented the interpretation of seismic horizons (Fig. 7).

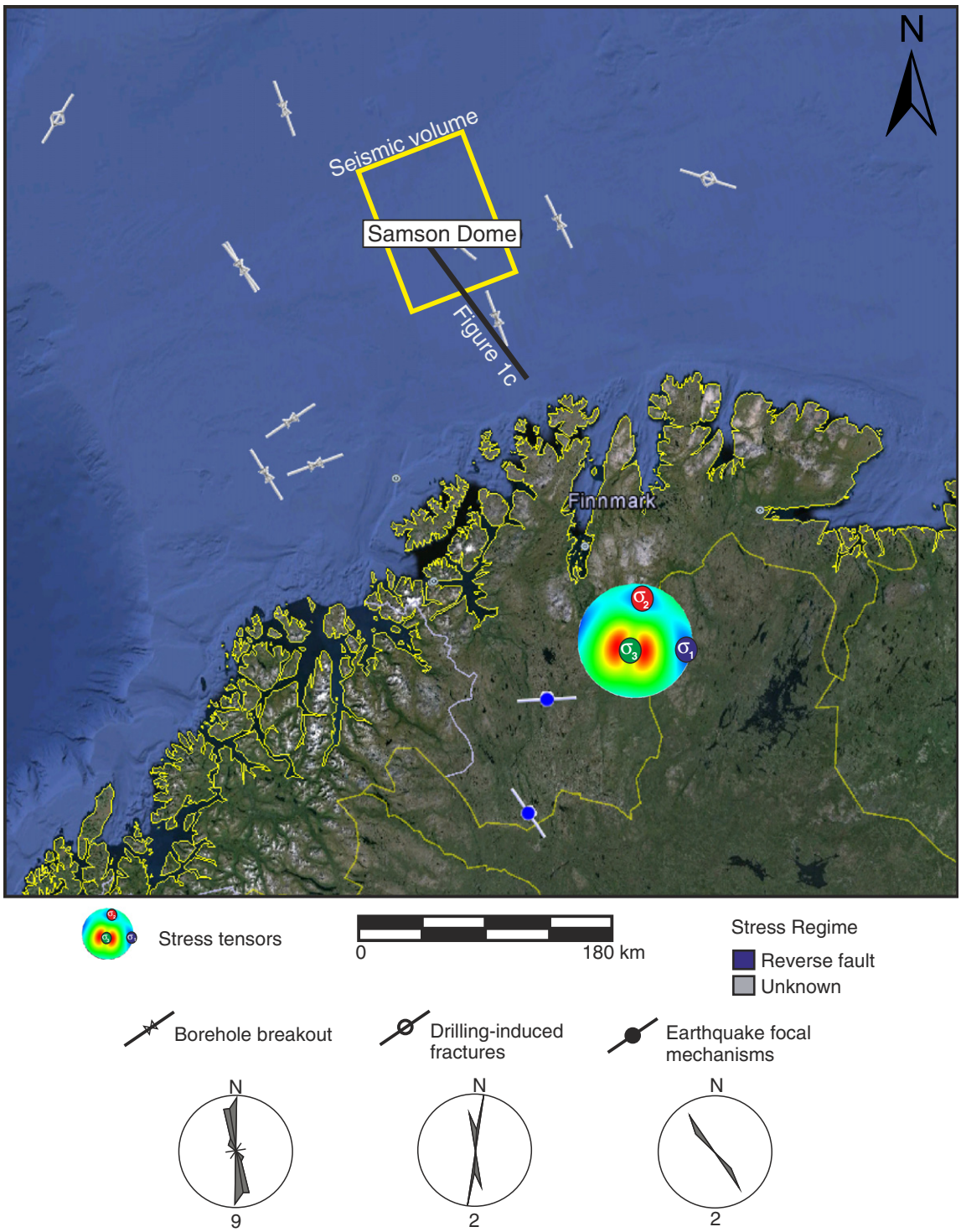

Fig. 3. Present-day stress data for the Barents Sea and Finnmark. Stress tensors for the Finnmark Platform were used to assess slip tendency and leakage factors for faults in the study area. Rose diagrams show the azimuth of the maximum stress σ_{Hmax} for each measurement technique. Stress data compiled from the World Stress Map (Heidbach et al., 2008).

3.1. Structural data

We mapped one hundred and thirty three (133) faults imaged on seismic sections and coherence data obtained from Petrel®. Coherence is a geophysical attribute calculated through the conversion of seismic-amplitude volume into a discontinuity volume. Coherence maps highlight the most prominent discontinuities in 3D seismic volumes, such as faults and fractures (Brown, 2011). Fig. 8 shows a coherence slice at a depth of −980 ms, where three distinct groups of faults were defined based on their geometry and orientation. Eight representative faults (F1 to F8) are highlighted on the coherence slice in Fig. 8 and were later used to obtain the displacement-length (D-x) and throw-depth (T-z) data in Figs. 9 and 10.

Displacement data provide insights into the mechanism of initiation, growth and evolution of faults through time (e.g. Cartwright et al., 1998). Displacement-length analyses consist of plotting the maximum displacement (D_{max}) of faults observed on seismic data relative to the

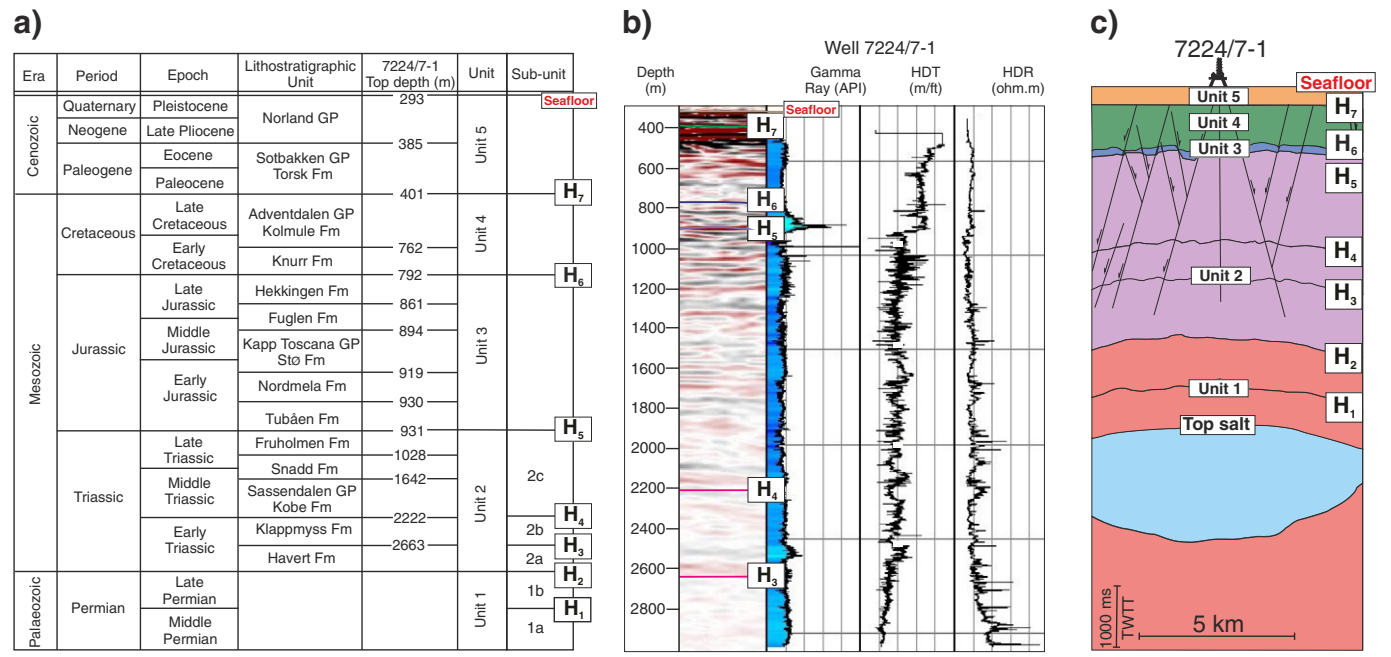

Fig. 4. Simplified stratigraphic column of the Ottar Basin showing the top depth for lithostratigraphic units crossed by well 7224/7-1. The interpreted horizons and respective seismic units are located to the right of this same column. Seismic horizons interpreted below well 7224/7-1 are also indicated. b) Interpreted seismic line and Gamma Ray, Density (HDT) and Resistivity (HDR) logs for the interval of interest in well 7224/7-1. c) Interpreted seismic section highlighting the interpreted seismic horizons, seismic units and faults.

length of the fault trace (Chapman and Williams, 1984; Dawers and Anders, 1995; Muraoka and Kamata, 1983; Nicol et al., 2002; Peacock, 1991; Pollard and Segall, 1987). Resulting D-x plots were created using Microsoft Excel®, with values converted to metres for both displacement and distance (Fig. 9).

Throw-depth profiles are helpful to estimate whether a fault has been reactivated (Baudon and Cartwright, 2008a, 2008b; Cartwright and Mansfield, 1998; Mansfield and Cartwright, 1996). In throw-depth profiles, reactivated faults show abrupt variations in throw gradients and magnitudes, whereas non-reactivated faults denote minor changes in their profiles and show comparatively smaller throw values (Baudon and Cartwright, 2008b). Throw-depth relationships were measured considering the difference between correlative seismic reflections on the hanging-wall and footwall of faults, in seismic sections orthogonal to the fault strike (Baudon and Cartwright, 2008b; Cartwright and Mansfield, 1998; Mansfield and Cartwright, 1996; Omosanya and Alves, 2014; Omosanya et al., 2015). Values for T-z plots were displayed in two-way travel time (ms TWTT) (Fig. 10).

Furthermore, the interpreted faults were imported to Midland Valley's Move® as 3D-mesh surfaces and filtered for edge triangles. Key attributes such as the true dip and azimuth for each fault vertex were created on Move® through the *Attribute Analyser Toolbar*. Because azimuth was calculated, the strike was also automatically calculated for each fault. The fault surfaces were then individually imported into 3D Stress® for stress modelling.

Fault analyses were performed to assess the orientation and the distribution of tectonic stresses across the study area (Morris et al., 1996). After mapping 133 faults, the stress inversion method developed by M^{c}Farland et al. (2012) was used to determine the principal paleostress tensors associated with these same faults. In this method, a fault is likely to slip when the shear stress is equal or greater than the normal stress acting on a fault surface (Morris et al., 1996). M^{c}Farland et al. (2012) indicate two important criteria that need to be taken into account to assess the quality of fit for stress tensors. They are: a) an expected positive relationship between slip tendency and displacement, and b) the small displacements with large slip tendency being more plausible than large displacements with small slip tendency i.e., surfaces may have started slipping at different points in time in this example.

We went a step further by modelling the tendency of faults to slip and leak fluids (Figs. 11 and 12). The *Stress Analysis Module* allows the colour-scaled 3D visualisation of the fault planes that are more likely to reactivate and leak. The workflow followed to obtain 3D models for slip tendency (Fig. 11) and leakage factor (Fig. 12) utilised the magnitudes and azimuths of present-day stresses for the Finnmark Platform provided by the World Stress Map (Heidbach et al., 2008). Data from the World Stress Map indicate compressional regimes at shallow depths, giving σ_1 as σ_{Hmax}, σ_2 as σ_{hmin}, and σ_3 as σ_v for present-day stress conditions in the study area (Fig. 3).

Slip tendency (T_s) comprises the likelihood that a fault will slip, computed as the ratio of shear (τ) to normal (σ_n') stresses on a fault plane, as shown in Eq. (1) (Morris et al., 1996). Slip tendency has no units and mathematically denoted as:

$$T_s = \tau/\sigma_n'. \quad (1)$$

Slip tendency depends on the stress field and orientation of a fault surface. A fault will slip depending on the cohesive strength of the surface and the coefficient of static friction (μ). For a cohesionless fault surface, a slip will occur when the resolved shear stress (τ) is equal or surpasses the frictional resistance to sliding (F), as shown in Eq. (2) (Morris et al., 1996):

$$F \leq \tau = \mu\sigma_n \quad (2)$$

Leakage factor (L) allows the quantitative modelling of the fluid transmissivity of faults, identifying faults that either constitute migration conduits for sub-surface fluid or, instead, act as local seals. The likelihood for cohesive surface to transmit fluids is defined as the ratio of the fluid pressure (P_f), considered to be hydrostatic and obtained through vertical stress data (Zoback, 2010), to the difference between

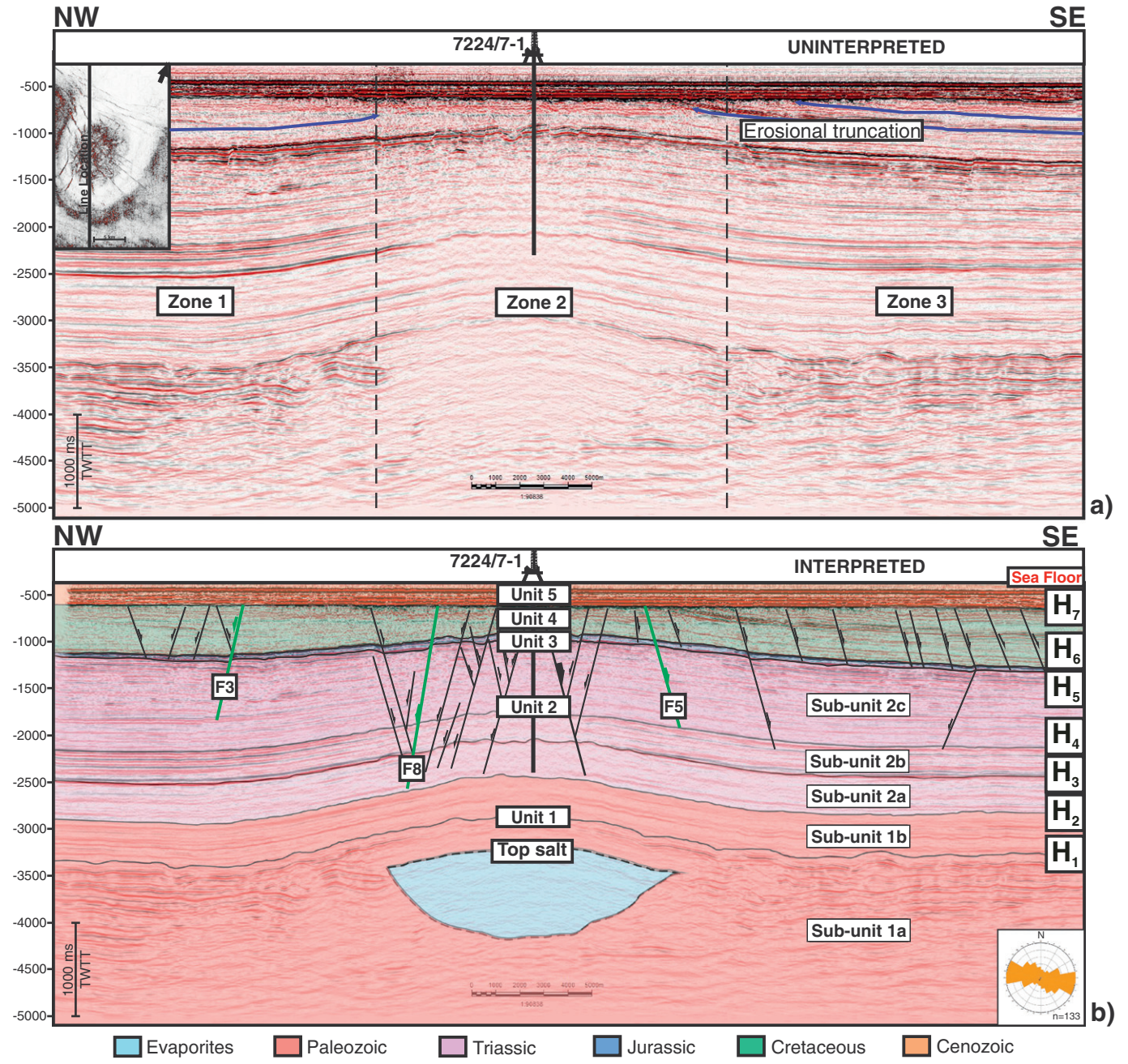

Fig. 5. a) Uninterpreted SE–NW seismic inline across the Samson Dome. The dashed lines indicate the subdivision of the study area into three distinct zones. b) Interpreted section showing the interpreted seismic units and horizons and some of the faults observed in the study area. Representative faults F3, F5 and F8, used in the D-x and T-z analyses, are identified in the figure. This section comprises an anticline with units of relatively constant thickness, with the exception of Late Cretaceous strata (Unit 4), which is truncated over the crest of the Samson Dome. The location of well 7224/7-1 is also indicated in this section. The rose diagram indicates the strike orientation of all 133 faults mapped in the study area. The location of the seismic section is shown at the bottom of the figure.

the normal stress (σ_n') and the tensile strength (T) of a fault zone (Midland Valley, 2014) such as:

$$L = P_f/(\sigma_n'\text{-}T) \quad (3)$$

The workflow to obtain the leakage factor values in the *Stress Analysis Module* is similar to the workflow for slip tendency. The magnitudes and azimuths from present stress data for the Finnmark Platform (Heidbach et al., 2008) were used together with a fluid pressure (P_f) value of 11 MPa, obtained considering the depth of borehole breakouts (1108 m) and the water column (296 m) above the seafloor (Fig. 12). The data in Figs. 11 and 12 show normalised slip tendencies (τ/τ_{max}) and leakage factors (L/L_{max}) so that calculated values fall within a range of 0.0 to 1.0.

4. Seismic interpretation

The eight (8) seismic horizons interpreted in this study are shown in Fig. 4 and Table 1. These horizons correspond to the tops of the Lower Triassic Havert and Klappmyss Formations, the Upper Triassic Fruholmen Formation, the Upper Jurassic Hekkingen Formation, the Upper Cretaceous Kolmule Formation and the Pleistocene Nordland Group in well 7224/7-1. Furthermore, the eight horizons were grouped into five sedimentary units from the Permian (Unit 1) to the Paleogene-Quaternary (Unit 5), according to their internal character and the

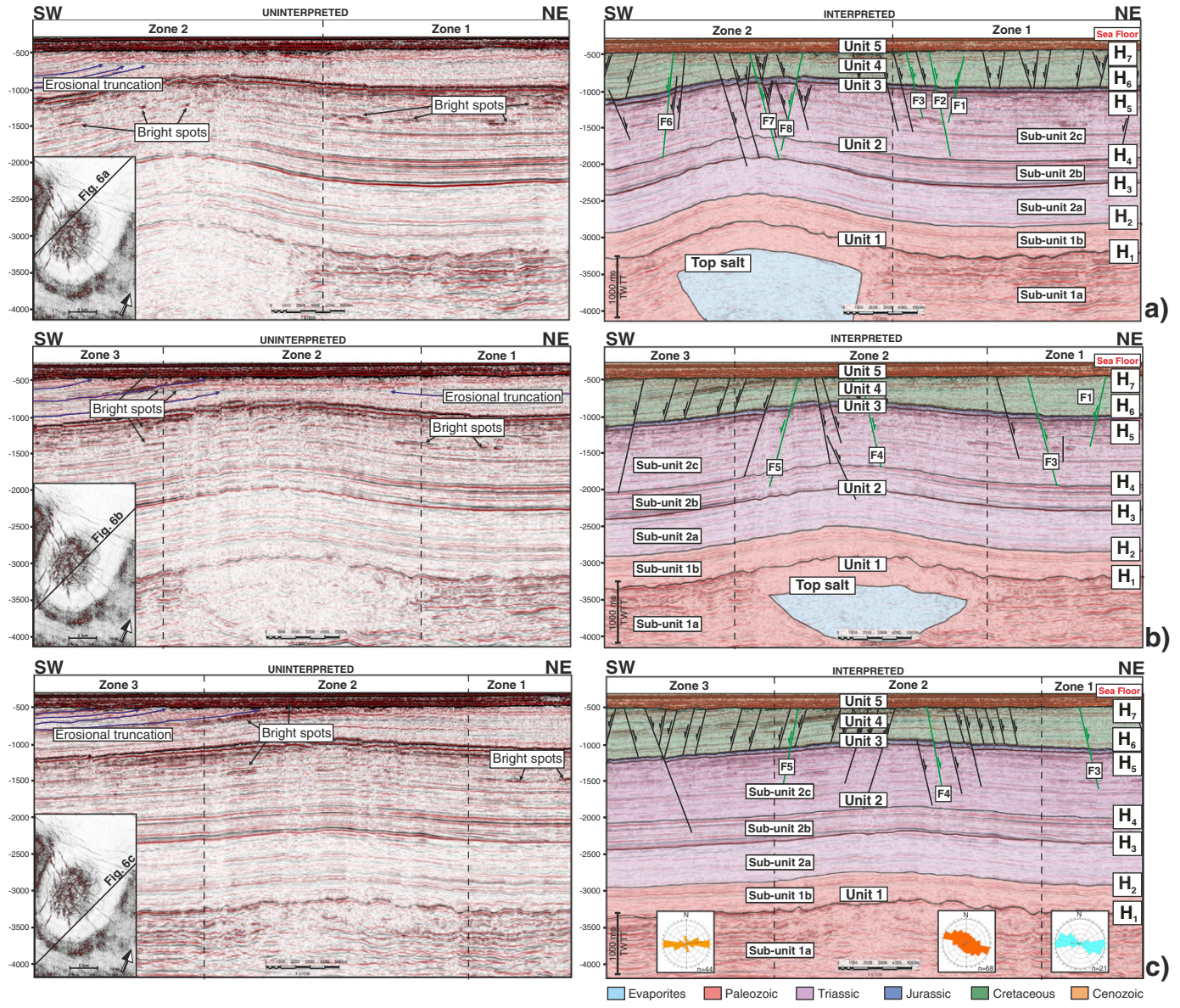

Fig. 6. Uninterpreted SW–NE seismic lines and corresponding interpreted sections for each of the three interpreted fault zones. Brightspots are indicated in the uninterpreted seismic sections. The eight representative faults (F1 to F8) used for the D-x and T-z plots in Figs. 9 and 10 are highlighted. a) Seismic line displaying Zones 2 and 1. This line is the most affected by the growth of the Samson Dome and exhibits a succession of asymmetric tilt-blocks in Zone 2. In Zone 1, large faults offset strata from the Paleozoic to Triassic. Faults confined to horizon H_1 are also observed in Zone 1. Representative faults F6, F7 and F8 occur in Zone 2, while Faults F1, F2 and F3 are found in Zone 1; b) Seismic line showing the three (3) zones defined for the study area and the location of faults F5 and F4 (Zone 2) and F1 and F3 (Zone 1); and c) Seismic line showing the three (3) structural zones in an area less affected by the Samson Dome. An NE-dipping fault segment offsetting horizons H_4 and H_5 is observed in Zone 3. Faults F5 and F4 occur in Zone 2. Fault F3 is interpreted in Zone 1. The rose diagram indicates the strike orientation of all faults mapped in each zone. The location of the seismic sections is indicated at the bottom of the figure.

geometry of the seismic reflections. The Middle and Late Permian horizons H_1 and H_2 were not intersected by well 7224/7-1. Hence, they were picked based on their acoustic impedance contrast and data from previous workers in the area such as Alves (2016); Breivik et al. (1995); Ehrenberg et al. (1998); Glørstad-Clark et al. (2010); Larssen et al. (2002) and Nilsen et al. (1993). Younger Permian strata were correlated with regional unconformities crossed by well 7124/3–1 (Figs. 1c, 4 to 6).

4.1. Unit 1 (Permian)

Unit 1 comprises two sub-units (1a and 1b) bounded by Mid Permian (H_1) and Late Permian (H_2) unconformities (Figs. 4–6). The Mid Permian horizon (H_1) is marked by a high-amplitude, positive reflection at a depth of approximately 4230 m (Fig. 4, Table 1). Strata in sub-unit 1a consist of grainstones and packstones rich in foraminifera and algae (Ehrenberg et al., 1998). Carbonate buildups occur in sub-unit 1a and are shown as high-amplitude wavy reflections. These structures are also observed on the thickness map in Fig. 7a. Carbonate build-ups were deposited in relatively shallow basinal environments together with variable amounts of anhydrite (Nilsen et al., 1993). Below the build-ups, a lenticular structure observed both in section (Figs. 5 and 6) and map view (Fig. 7a) consists of an evaporitic body recognised due to the loss of internal seismic reflections. The Mid Permian sub-unit 1a corresponds to the boundary between Seismic Units II and III of Nilsen et al. (1993) and to the boundary between the Early Sakmarian unit L7 and the Late Sakmarian–Late Artinskian unit L8 of Ehrenberg et al. (1998). Sub-unit 1a is deformed over the main lenticular, evaporite body that forms the base of the Samson Dome (Fig. 7a).

The Late Permian horizon H_2 comprises a medium amplitude, positive seismic reflection (Figs. 5 and 6). This horizon is continuous and marked by the presence of a small amount of offsetting faults (Figs. 6a–c). Horizon H_2 coincides with the top of sub-unit 1b, which

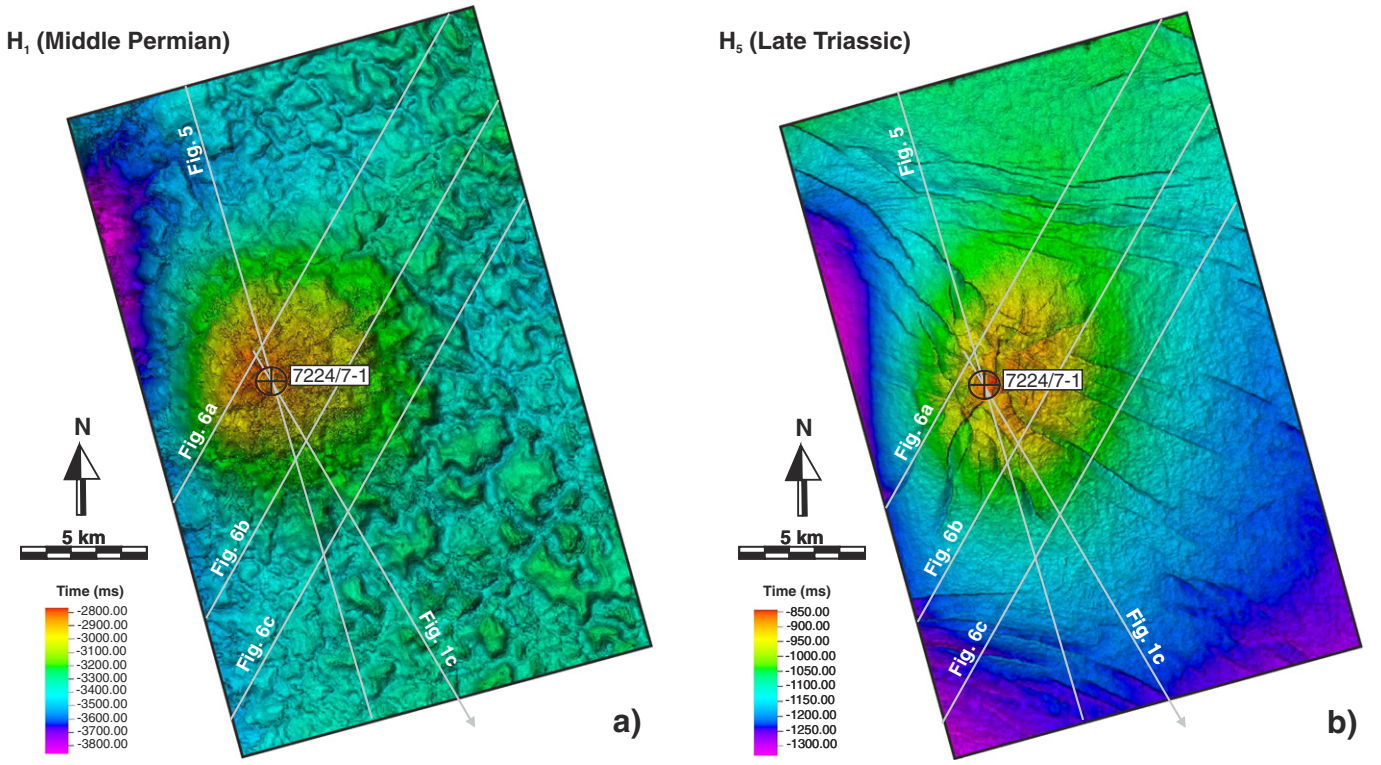

Fig. 7. Time-structural maps for a) horizon H_1 (Middle Permian) highlighting the occurrence of carbonate buildups at this stratigraphic level, and b) horizon H_5 (Late Triassic) showing the fault pattern both at the crest of the Samson Dome and more distally in the study area. The location of seismic sections interpreted in this work are displayed on both maps.

comprises calcareous silt shales, calcareous spiculites with clay matrix and shale lenses (Ehrenberg et al., 1998). Sub-unit 1b correlates with Seismic Unit IV of Nilsen et al. (1993) and to the Kungurian–Late Permian unit L9 of Ehrenberg et al. (1998).

4.2. Unit 2 (Triassic)

The lower boundary of Unit 2 coincides with H_2 (Figs. 4, 5 and 6) and comprises distinct Early Triassic (2a and 2b), and Late Triassic (2c) sub-units. Horizon H_3 coincides with the top of the Lower Triassic Havert Formation (Fig. 4, Table 1). This is the deepest horizon drilled by well 7224/7-1, at a depth of 2663 m (Figs. 4 and 5). Horizon H_3 is a negative seismic reflection with high amplitude. In areas surrounding the Samson Dome it is possible to observe a loss of continuity, probably resulting from a lower seismic resolution, as a small number of faults offsets horizon H_3 (Figs. 5 and 6). The 865 m-thick sub-unit 2a shows no major thickness variations throughout the study area, and consists of medium to dark-grey shales with minor intervals of pale grey siltstones and sandstones (Dalland et al., 1988; Larssen et al., 2002). Sub-unit 2a corresponds to seismic sequence S1 in Glørstad-Clark et al. (2010).

Horizon H_4 correlates with the top of the Klappmyss Formation, and occurs at a depth of 2222 m in well 7224/7-1 (Figs. 4 and 5). This horizon shows low amplitude and negative positive polarity and, similarly to horizon H_3, loses its continuity in areas close to the Samson Dome (Figs. 5 and 6). Below H_4, sub-unit 2b comprises a 441 m-thick stratigraphic interval with regular thickness, offset by faults around the Samson Dome (Figs. 5 and 6). However, faults are also observed away from this structure. Sub-unit 2b consists of dark-grey shales grading upwards into interbedded shales, sandstones and siltstones (Dalland et al., 1988). This sub-unit correlates with the Olenekian seismic sequence S2 of Glørstad-Clark et al. (2010) (Table 1).

One of the strongest negative reflections in Unit 2 is horizon H_5, which marks the top of Upper Triassic strata (Figs. 4 and 5). In well 7224/7-1, this reflection correlates with the top of the Fruholmen Formation, and occurs at a depth of 931 m (Fig. 4a). Horizon H_5 marks the top of the 1291 m-thick sub-unit 2c, which includes the Fruholmen (97 m thick), the Snadd (614 m thick) and the Kobe Formations (580 m thick) (Figs. 4–6). The lithology of these three formations is similar, comprising grey to dark shales grading upwards into interbedded sandstones, shales, siltstones and coal (Dalland et al., 1988; Larssen et al., 2002). The Fruholmen Formation shows no discernible thickness variations (Figs. 5 and 6). Sub-unit 2c is mainly faulted over the salt dome, but faults are also observed away from this structure. A small number of bright spots are observed in sub-unit 2c (Fig. 6). This sub-unit is equivalent to the top of the Upper Triassic S5 unit of Glørstad-Clark et al. (2010) (Table 1).

4.3. Unit 3 (Jurassic)

Unit 3 has an upper boundary at the top of the Late Jurassic horizon H_6, which coincides with a reflection of negative amplitude (Figs. 4 to 6). In well 7224/7-1, this reflection corresponds to the top of the Hekkingen Formation and occurs at a depth of 792 m (Fig. 4). Unit 3 is an interval comprising brownish grey to dark grey shales and claystones with minor thin amounts of limestone, dolomite, siltstone and sandstone (Dalland et al., 1988). This thin (139 m) interval has a regular thickness and is markedly faulted (Figs. 5 and 6). Faulting causes this horizon to be discontinuous around the Samson Dome (Figs. 5 and 6).

4.4. Unit 4 (Cretaceous)

Unit 4 is bounded at its base by horizon H_6 and at its top by horizon H_7, a Late Cretaceous unconformity occurring at a depth of 401 m below the seafloor in well 7224/7-1 (Fig. 4). Horizon H_7 is a positive and high-amplitude reflection, which coincides with the top of the Kolmule Formation (Fig. 4a). The horizon is truncated over the crest of the Samson Dome (Figs. 5 and 6) and, comprises the most faulted seismic-stratigraphic marker in the study area (Fig. 7b). A few distinctive bright spots occur close to the top of Unit 4 (Fig. 6b). In well 7224/7-1, the Unit 4 thickness reaches 391 m and includes the Knurr and Kolmule

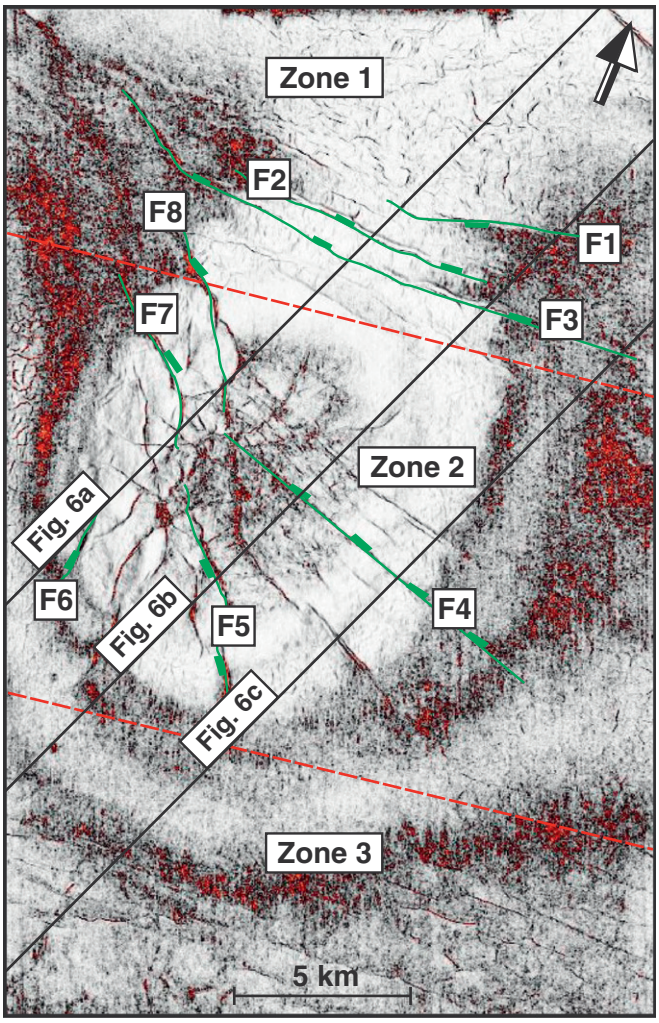

Fig. 8. Coherence slice at Z = −980 ms crossing the Samson Dome, which is subdivided into three distinct zones. Green lines represent the location of the eight representative faults interpreted in D-x and T-z plots (see Fig. 9).

Formations (Fig. 4). The Lower Cretaceous Knurr Formation, 30 m thick, comprises dark-grey shales and red to yellow-brown claystones at its top (Larssen et al., 2002). In parallel, the Kolmule Formation is about 361 m-thick and is composed of brownish grey to dark grey shales, interbedded with occasional intervals of siltstone and sandstone (Dalland et al., 1988; Larssen et al., 2002). The Kolmule Formation is Early to Late Cretaceous in age.

4.5. Unit 5 (Paleogene — Quaternary)

On the interpreted seismic sections, the top of Unit 5 coincides with the modern seafloor (Fig. 4). This Paleogene to Quaternary unit is 108 m-thick and shows continuous and high-amplitude reflections at its base and top. Low-amplitude and discontinuous reflections are observed in Unit 5, hindering the mapping of faults in its interior. Discrete high-amplitude anomalies are observed on seismic data and are interpreted as bright spots (Figs. 5 and 6).

Unit 5 comprises the Nordland and Sotbakken Groups (Fig. 4). The Nordland Group consists of marine sand and clays grading to sandstones and claystones (Dalland et al., 1988; Glørstad-Clark et al., 2010). Clays are grey to greyish green, blocky, locally silty and non-calcareous. The softness of the clays from Nordland Group is a distinctive feature when comparing to the claystones from the underlying Sotbakken Group (Dalland et al., 1988) (Fig. 4).

5. Fault distribution on the Samson Dome

The structural interpretation of a coherence slice from a depth of −980 ms resulted in the sub-division of the study area into three distinct zones (Fig. 8). The sub-division is done based on the density, geometry, and orientation of the interpreted faults. Fault density is greater over the Samson Dome (Zone 2) and decreases towards the southeast and northwest in Zones 1 and 3 (Fig. 8). Most faults developed away from the Samson Dome are restricted to Unit 4 (Cretaceous). However, a considerable number of faults also extend into the Triassic Unit 2 (Figs. 5 and 6).

5.1. Zone 1

Zone 1 occurs to the northwest of the Samson Dome (Fig. 8). The mean strike direction for the 21 faults mapped in this zone is ENE, with the largest faults striking E (see rose diagram in Fig. 6). Zone 1 is not located on the Samson Dome, but this broad anticline still influences its structural configuration (Fig. 6). Small-scale bright spots were also identified below horizon H_5 (Fig. 6).

One of the distinctive features in Zone 1 is the presence of a vertical fault segment offsetting Triassic strata, in which a SW-dipping fault segment (F1) is visible (Fig. 6a). In Fig. 6b, a small vertical fault segment is also interpreted within Upper Triassic strata. Apart from this latter fault types, no other evidence for vertical faults indicating strike-slip movements was found in Zone 1. With the exception of fault F1 the deepest offsetting faults in Zone 1 dip all to the NE. Faults that occur at Cretaceous level (Unit 4) dip both to the SW and NE (Figs. 6 and 8).

5.2. Zone 2

Zone 2 is located in the central part of the study area and comprises faults developed on the crest of the Samson Dome (Fig. 7). Zone 2 is the most deformed of the three interpreted zones and includes deeply seated faults such as F5, which offset Upper Permian to Upper Cretaceous strata (Fig. 6). Significantly, the top of Upper Cretaceous strata shows evidence of erosional truncation (Figs. 5 and 6).

In Zone 2, the predominant strike for faults is NW-SE. However, NE–SW striking faults are also interpreted (Fig. 6). Close to the Samson Dome, sub-units 2b, 2c, Unit 3, and Unit 4 are highly faulted with a succession of tilt-blocks (Figs. 6a and 6b). These structures are asymmetric and limited by synthetic and antithetic faults (Fig. 6). Relatively large tilt-blocks are observed in Fig. 6b. The tilted blocks are delimited by F4 to the NE and by other fault segments to the SW. These fault segments extend from the top of the Lower Triassic to the top of Upper Cretaceous strata (Figs. 5 and 6). Away from the Samson Dome, it is possible to see a large tilt-block where all the faults located to the right of the seismic section dip to NE (Fig. 6c). Faults located on the left of this section dip to the SW (Fig. 6c).

In addition, bright spots were interpreted in Zone 2 below horizon H_5 (Fig. 6a). In Fig. 6b, the bright spots occur in Upper Cretaceous strata near the base of Unit 5.

5.3. Zone 3

Zone 3 is located in the southernmost part of the study area and comprises large faults that offset sub-unit 2b to Unit 4 (Fig. 8). Most of the faults in this zone are, however, contained within Upper Cretaceous strata in Unit 4. Faults in Zone 3 strike in an E-W direction (Fig. 6). As faults predominantly dip to the SW, the main distinctive feature of Zone 3 is the occurrence of a NE-dipping segment between horizons H_4 and H_7 (Fig. 6c). Two faults within Unit 4 intersect this latter fault segment. Relative to the other two zones, Zone 3 show little connection to the Samson Dome. Several bright spots are also observed below horizon H_5 and close to the seafloor in this zone (Fig. 6).

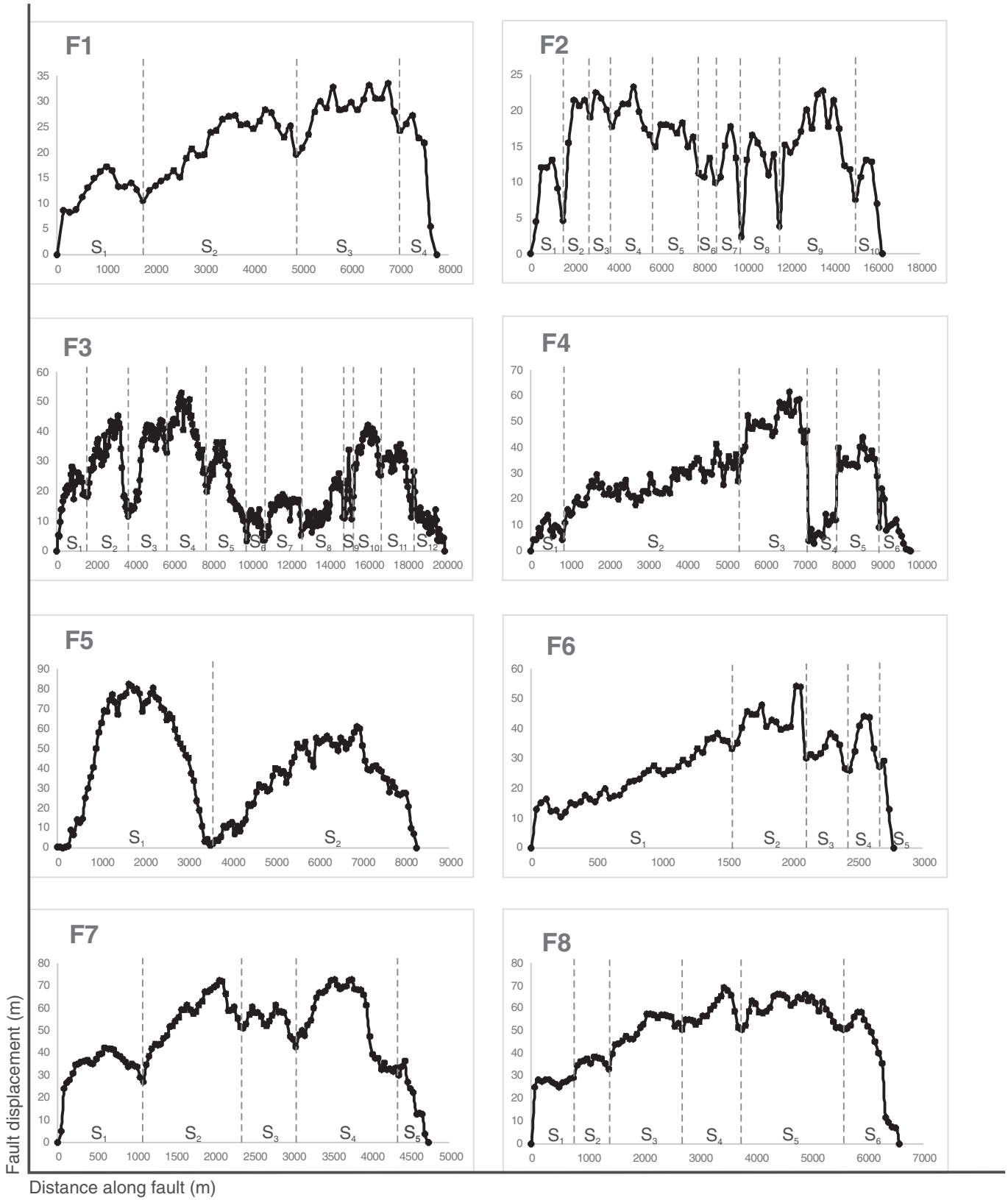

Fig. 9. Displacement-length (D-x) plots for eight representative faults in the study area. Faults are classified as C- and M-types according to their profiles (Muraoka and Kamata, 1983), as later described in this work. Displacement curves were created along horizon H_5 (Late Triassic). The grey lines indicate minimum displacements and segment linkage. Fault displacement and distance along the fault length are displayed in metres. Dotted lines and S_1 to S_n denote distinct fault segments later linked to form a continuous fault plane.

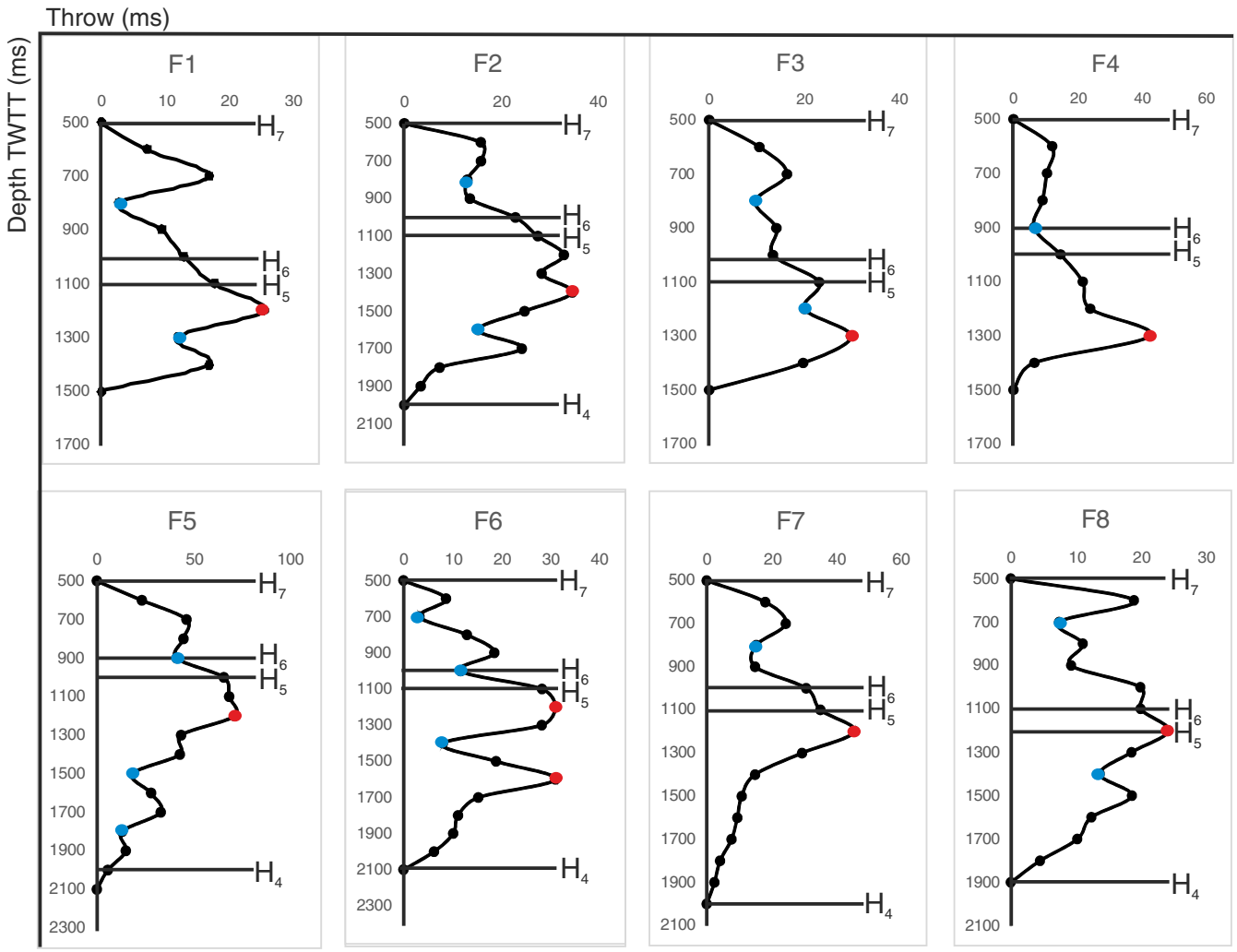

Fig. 10. Throw-depth profiles for eight representative faults with both depth and throw measured in ms. Three throw profiles were identified: asymmetric, M-type and skewed M-type. Black lines indicate the horizons cut by the faults. The maximum throw for the majority of the faults occurs at horizon H_5 (Late Triassic). Throw maxima are indicated by red dots and the blue dots highlight the minimum throw values.

6. Fault displacement analyses

6.1. Main fault families

The interpreted faults are divided into distinct families; named types A to C. Type A faults are crestal faults located on the crest of the Samson Dome (Fig. 6a). They form small-scale graben, half-graben and horst structures, and show predominant NW to ENE strikes and an average dip of 39°. Faults F4 to F8 are examples of faults in this category. Type A faults chiefly occur in Zone 2 where the Samson Dome is located, but they may also extend to Zone 1 e.g., faults F7 and F8 (Fig. 8). These faults are among the deepest in the study area, occurring from Lower Triassic to Upper Cretaceous strata (Fig. 6).

Type B faults are located away from the Samson Dome and consist of near-parallel faults with predominant E-W strikes and dips ranging from 33° to 48°. In the study area, Type B faults show no evidence for strike-slip movement. Faults F1 to F3 are examples of Type B faults (Figs. 6 and 8). Fault F3 is the largest fault in the study area, with a length of around 20,000 m (Fig. 8). This fault offsets Upper Triassic to Upper Cretaceous strata i.e. from horizons H_4 to H_7 (Fig. 6b). F3 also delimits a bright spot in Zone 1 (Figs. 6a and b).

Coherence data in Fig. 8 show Type C follow a pattern that resembles polygonal fault systems (Cartwright, 1996; Lonergan et al., 1998). Type C faults are observed within Cretaceous strata (Unit 4) and have a predominant strike direction to the NW (Figs. 3 and 6). Faults striking NE are also found. The dips for these faults are variable, ranging from 29° to 52°.

Time-structure data for horizon H_5 (Fig. 7b) and the profiles in Fig. 10 show that interpreted faults can display average throw values ranging from 12 to 33 ms on the Samson Dome. The greatest throw values occur for fault F5, where a throw maximum of 68 ms is observed (Fig. 10). Seismic profiles, however, do not exhibit significant thickness variations along most of the interpreted horizons (Fig. 6). Only strata older than the Late Cretaceous Unit 4 show significant thickness variations.

6.2. Interpretation of displacement-length (D-x) plots

Fig. 9 shows displacement-length (D-x) plots for the eight representative faults. The shapes of D-x plots relate to the observed displacement variations. For a single and isolated fault, D-x profiles will exhibit triangular or flat-topped shapes representing a near-symmetric slope with gentle variations in displacement (Childs et al., 1995; Muraoka and Kamata, 1983; Nicol et al., 1996; Peacock and Sanderson, 1991). These are the C-type faults of Muraoka and Kamata (1983) and represent deformation in soft, homogeneous layers. Faults with abrupt variations in displacement indicate linkage of individual fault segments through the displacement minima (Nicol et al., 1996; Walsh et al., 2003). Their

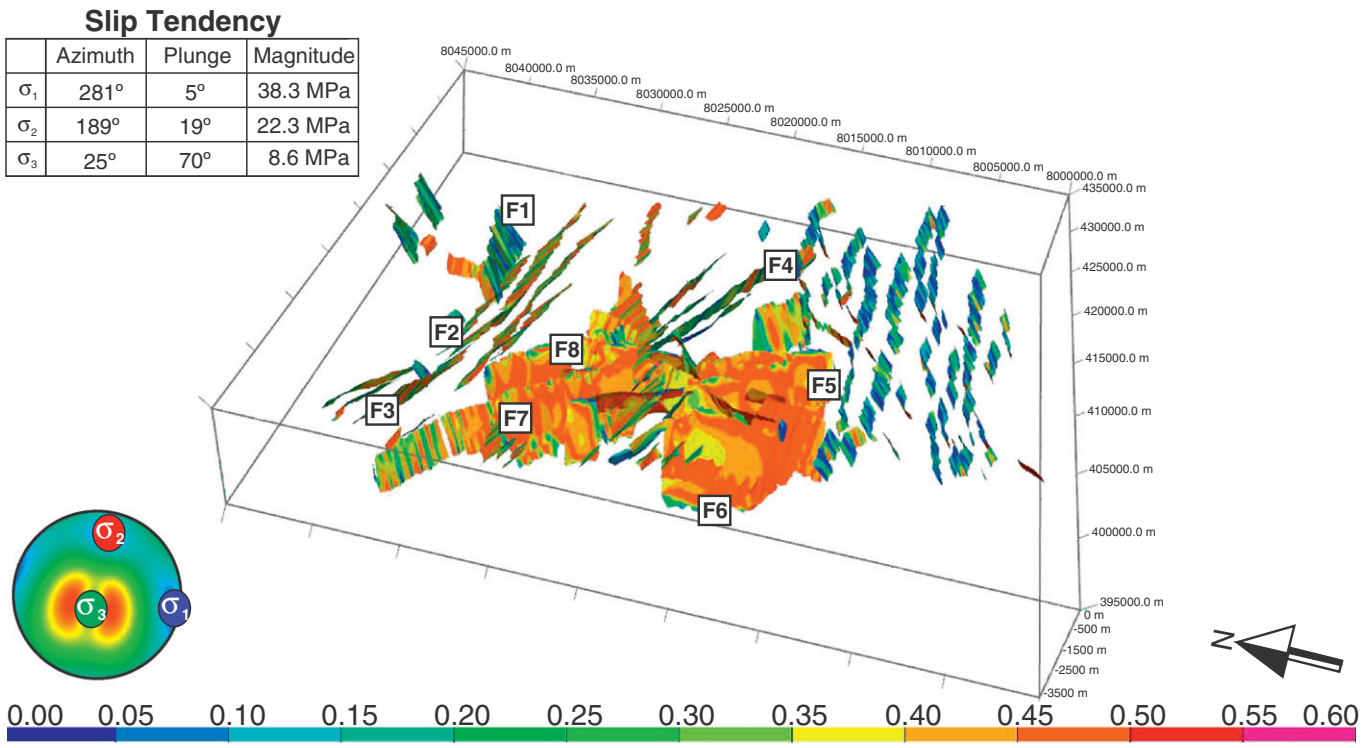

Fig. 11. Slip Tendency model for faults in the study area, considering present-day stress data from Finnmark. The colour scale shows normalised slip tendency T_s/T_{max}. Slip tendency values range from 0 to 0.6, with faults in Zone 2 showing the highest values and a decrease in the slip tendency towards their upper tips. In Zones 1 and 3, slip tendency varies between 0.3 and 0.5.

corresponding profiles show a broad central section with no significant slope variations, and flanking portions with an abrupt displacement change, thus resulting in a marked asymmetric character. These structures are classified as M-type faults, reflecting deformation in rigid units (Muraoka and Kamata, 1983).

Displacement-length (D-x) plots for Type A and Type B faults are provided in Fig. 9. Overall, the geometry of the D-x profiles vary from asymmetric (F1, F3, F4, F5, and F6) to symmetric (F2, F7, and F8). Faults F7 and F8 have distinctive M-type profiles. The other faults have more complicated displacement profiles. For example, profiles for faults F1

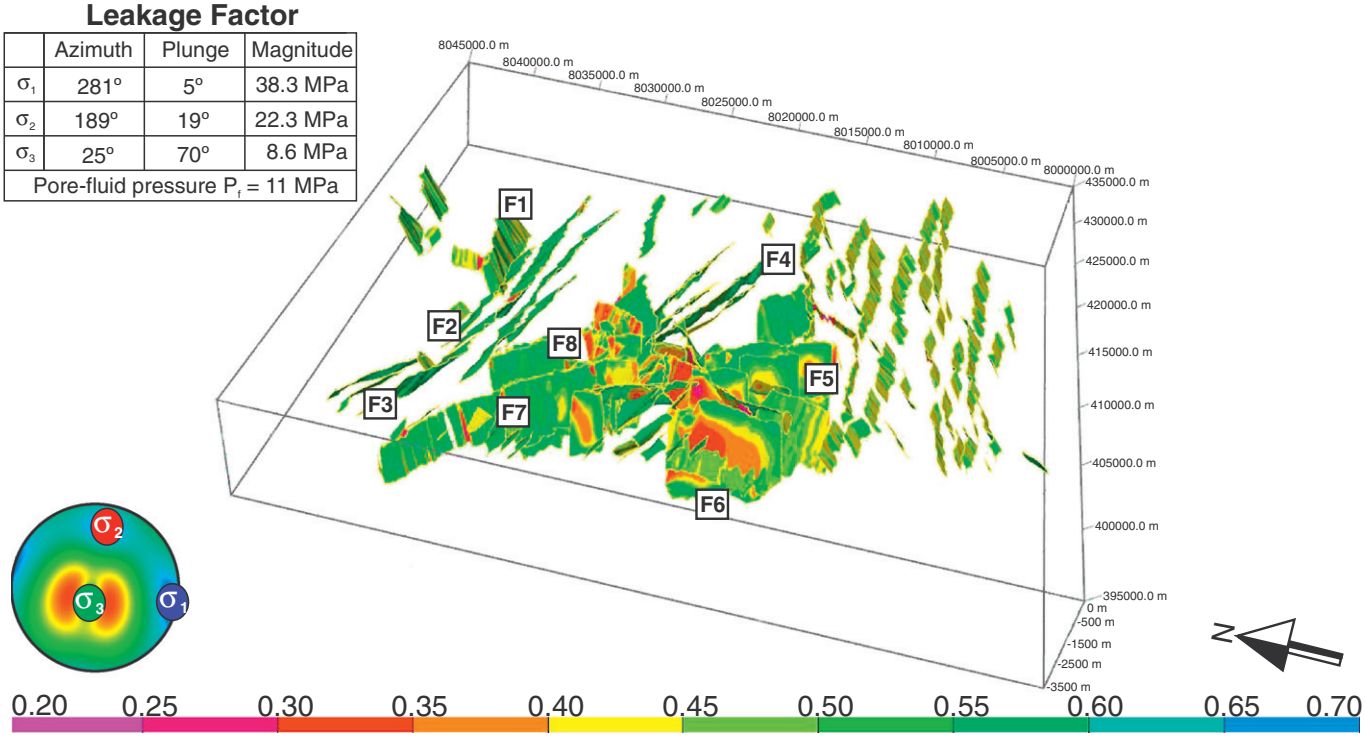

Fig. 12. Leakage Factor model for faults in the study are considering present-day stress data from Finnmark. The colour scale shows normalised Leakage Factor L/L_{max}. Leakage factors for the study area range from 0.2 to 0.85. For Zone 2 these values are greater towards the upper tip of the faults, decreasing with depth.

Table 1
Seismic character and lithologies of the seismic units interpreted in the study area. Correspondence of the seismic units in this work with the seismic sequences in the literature: [a](Glørstad-Clark et al., 2010); [b](Ehrenberg et al., 1998); [c](Nilsen et al., 1993).

Epoch	Seismic unit	Seismic sub–unit	Horizon	Thickness (m)	Internal character, geometry and terminations	Lithology (Larssen et al., 2002; Dalland et al., 1988)	Seismic sequences in the literature
Pleistocene	5		Seafloor	108	Discontinuous reflections close to the seafloor. No mapped faults in this unit. Occurrence of bright spots is frequent.	Sands and clays grading into sandstones and claystones	
			H_7				
Late Cretaceous	4			391	Strong amplitude and high–frequency positive reflections. Horizon H_7 is truncated on the crest of the Samson Dome. Large and shallow amplitude anomaly cut by faults.	Brownish grey to dark grey shales and claystones interbedded with occasional limestone, siltstone and sandstone	
			H_6				
Late Jurassic	3			139	Strong amplitude and high–frequency negative seismic reflections. Offset by faults. Discontinuous reflections on the Samson Dome.	Basal and top shales interbedded with siltstones and sandstones	
			H_5				
Late Triassic	2	2c		1291	Strong to moderate and high to medium frequency negative reflections. Offset by faults. Discontinuous reflections on the Samson Dome.	Basal grey to dark shales grading upwards into interbedded sandstones, shales and coals	S5[a]
			H_4				
Early Triassic		2b		441	High amplitude and positive reflections. Constant thickness throughout the study area. Offset by faults on the Samson Dome and away from this structure.	Dark grey shales grading upwards into interbedded shales, sandstones and siltstones	S2[a]
			H_3				
		2a		1537	High amplitude negative reflection. Loss of seismic resolution close to the dome. Seismic reflections offset by faults on the Samson Dome.	Medium to dark grey shales with minor intervals of siltstones and sandstones	S1[a]
			H_2				
Late Permian	1	1b		4200	Low–to moderate–amplitude internal and positive reflections. Continuous over the study area. Not intersected by faults.	Calcareous silty shales, calcareous spiculites with clay matrix and shale lenses (Ehrenberg et al., 1998)	L9[b] Unit IV[c]
			H_1				
Middle Permian		1a		5500	Strong amplitude and positive reflections. Wavy towards the top of the unit. Loss of seismic resolution close to the dome. Not intersected by faults.	Carbonates interbedded with the evaporitic (lenticular) body	L7–L8[b] Unit II–Unit III[c]

and F6 are skewed to the right (Fig. 9). Fault F5 is a combination of two distinct C-type profiles. Fault F4 include an M-type profile to the left and a C-type to the right (Fig. 9). Fault F2 displays the most complicated D-x profile with combination of several types of C-, M- and skewed-type profiles. The complex D-x profile points to lateral segmentation of the faults (Muraoka and Kamata, 1983; Nicol et al., 1996), an evidence that these faults were not isolated during their propagation and growth. For example, Fault F5 developed by combination or linkage of two disparate and initially isolated faults (cf. Childs et al., 1995; Peacock and Sanderson, 1991). Hence, the most laterally segmented fault is F3, with twelve (12) segments, followed by F2 with ten (10) segments. Fault F8 and F4 have six (6) segments each, whereas faults F6 and F7 have five (5) segments. Fault F1 consists of four (4) segments and the least segmented fault is F5, with two (2) segments (Fig. 9).

Apart from fault segmentation, the representative faults also have variable maximum displacement (d_{max}) and fault length (Fig. 9). D_{max} ranges from 81 m (F5) to 23 m (F2), while fault length varies from about 2.8 km (F6) to 20 km (F3). The point of maximum displacement for a fault may coincide with their point of nucleation (cf. Barnett et al., 1987; Nicol et al., 1996; Walsh and Watterson, 1987), but this assertion will only be true for isolated blind faults or faults that show less segmentation. In terms of their connection to the Samson Dome, the Type A faults (crestal) have length that are lesser than those of Type B. The longest faults are located on the margin of the Samson Dome. However, Type A faults have higher D_{max} relative to the Type B faults.

6.3. Interpretation of throw-depth (T-z) plots

The throw-depth (T-z) plots for the eight representative faults are shown in Fig. 10. These profiles include C-type (F1, F6 and F7), skewed M-type (F3 and F4), M-type (F2 and F8) and skewed C-type profiles (F5). Although the profiles can also be grouped into simpler types e.g., the profile for fault F1 is classified as an M-type, whereas F1 is interpreted here as a combination of two Type C profiles (Fig. 10).

Throw values generally increase with depth for faults F1, F3 and F4 (Fig. 10). A different geometry is observed for faults F2, F5 and F7, whose throws increase from their upper tips to a depth of about 700 ms. Displacement minima are recorded at 800 ms for faults F2 and F5, and at 900 ms for fault F5. The maximum throw occur at ~1200 ms towards the lower tip in faults F5 and F7, and at ~1400 ms in fault F2 (Fig. 10). Throw-depth plots for all the faults show that the maximum displacement occurs within Upper Triassic strata (Fig. 10). The T-z plots signify the complex vertical segmentation of the faults and likelihood of fault reactivation through dip linkage. This aspect is discussed further in Section 8.2.

7. Stress distribution, slip tendency and leakage factors for faults in the Samson Dome area

The styles of deformation in the Samson Dome area reflect a complex stress distribution. Stress inversions for all the faults indicate paleostress conditions similar to the initially expected, considering the high standard deviation for stress azimuths gathered from the literature. We, nevertheless, estimated a sub-horizontal σ_1, plunging 12° along a N130° azimuth. The orientation of σ_3 is sub-vertical, plunging 77.5° along an N298.4° azimuth. Earthquake focal mechanisms from the Finnmark Platform, located 339 km from the Samson Dome, also favour a compressional stress regime with a σ_3 plunging 70° along an N25° azimuth. The orientation of σ_1 is, based on focal data, sub-horizontal, plunging 5° along a N281° azimuth (Fig. 3).

Normalised slip tendency values for faults in the study area vary from 0.0 to 0.6 (Fig. 11). Most faults in Zones 1 and 3 (Type B and C faults) show slip tendency values between 0.3 and 0.5. Faults in Zone 2 (Type A faults) have the highest slip tendency values. In Fig. 11, one can note that some faults on the Samson Dome show a decrease in slip tendency from their lower to upper tips. Normalised Leakage factors were also calculated considering present-day stress states for Finnmark and a fluid pressure of 11 MPa, based on vertical stress measurements.

In this case, the leakage factor values obtained for the study area range from 0.20 to 0.85, with the most faults in the southern and northern parts of the study area showing leakage factors varying from 0.50 to 0.70 (Fig. 12). An interesting pattern is observed in Zone 2; some of the NW-SE trending faults show larger leakage factors close to their upper tips (Fig. 12). These values diminish along the fault with depth. The faults most prone to leak are the faults offsetting the shallowest strata on the crest of the Samson Dome (Fig. 12).

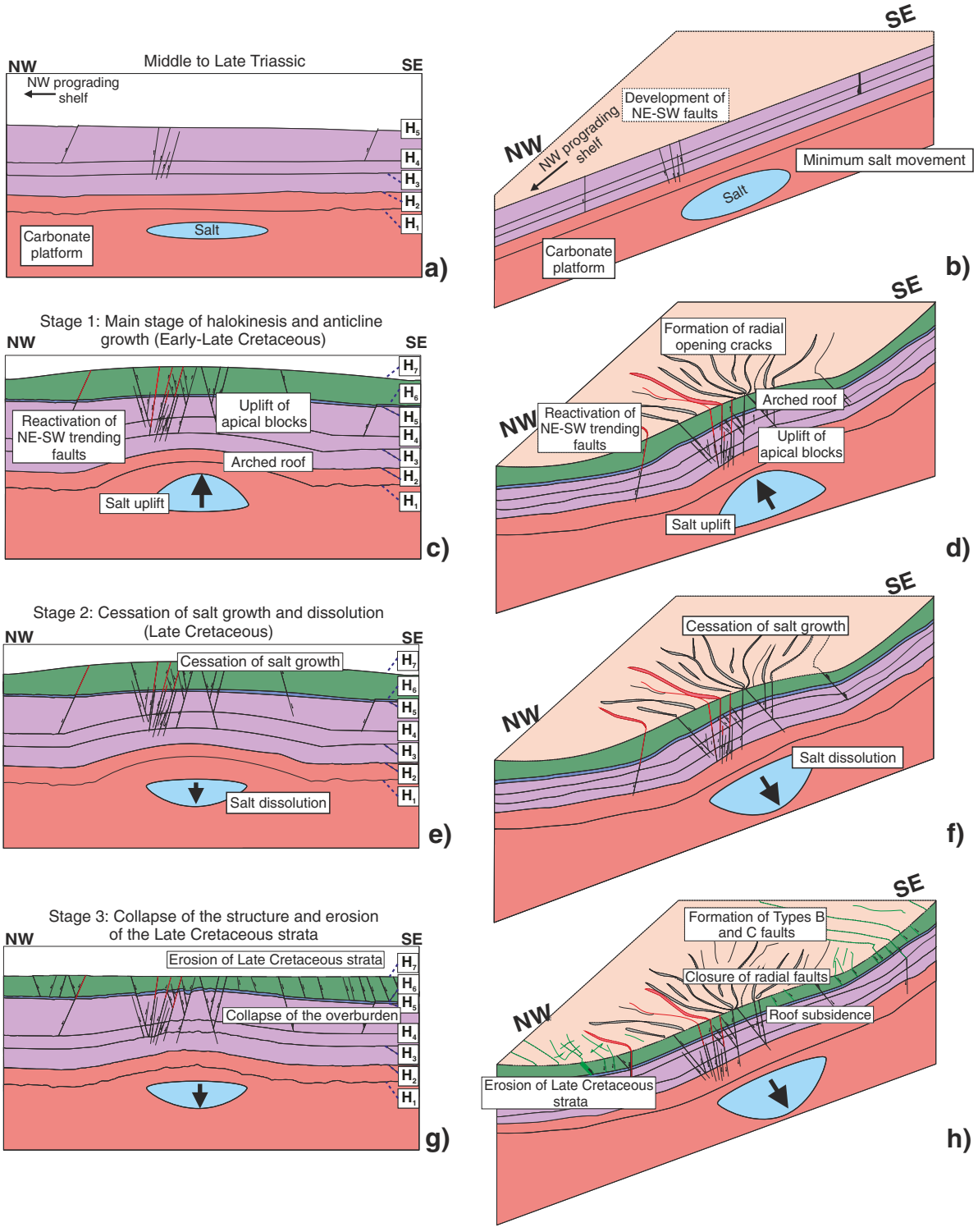

Fig. 13. Proposed evolution model for the Samson Dome area, with a 2D and 3D representation for each of the evolution stages considered in this paper. a) and b) During the Middle and Late Triassic a NW-prograding shelf reached the study area. However, the post-salt overburden was barely mobilised and the only structures developed at this period comprised a few NE–SW faults. c) and d) Main stage of halokinesis and anticline growth (Early-Late Cretaceous). In this stage, salt pierced the overburden causing the opening of radial faults and the reactivation of the NE–SW faults. e) and f) the second stage is characterised by the ceasing of the salt uplift in the Ottar Basin and caused the dissolution of the crest of the dome. g) and h) late dissolution of the salt dome caused the structure to collapse over its weight resulting in the formation of Types B and C faults, with closure of radial faults. During the Late Cretaceous–Paleogene transition an intensive erosional episode removed part of the overburden.

8. Discussion

8.1. Structural evolution of the Samson Dome and timing of faults

A conceptual model for the evolution of the Samson Dome is presented in Fig. 13. At a regional scale, the first halokinetic movements in the Ottar Basin took place from Middle to Late Triassic, resulting from differential loading imposed by NW-prograding shelf deposits and by the reactivation of basement faults (Breivik et al., 1995; Klausen and Mørk, 2014). However, considering that NW-prograding strata arrived to the Samson Dome area relatively late in the Triassic, and that thick carbonates cover the Upper Palaeozoic evaporites in the study area, we suggest that Middle to Late Triassic halokinesis barely deformed the post-salt overburden around the Samson Dome. The only evidence for important Middle to Late Triassic tectonics is the occurrence of a few NE-trending faults at the level of H_4 and H_5 (Figs. 5 and 13a–b). Examples of these NE-trending faults that reach the Triassic horizons are faults F5, F6 and F8 (Type A faults). These representative faults comprise maximum and minimum throw displacements between the Triassic Horizons H_4 and H_5, indicating that these fault segments were reactivated.

The interpreted 3D seismic cube indicates that the bulk of halokinetic movements occurred in the Late Mesozoic-Early Cenozoic. Faults formed during the Late Cretaceous in the Ottar Basin trend preferentially to the NW, whereas Middle to Late Triassic NE-trending faults were reactivated later. Extension in the Barents Sea, related to the opening of the North Atlantic Ocean, is likely to have caused the mobilisation of salt in the Ottar Basin and the subsequent reactivation of NE-trending faults (Faleide et al., 1993; Gudlaugsson et al., 1998; Safronova et al., 2014). Evidence for this salt mobilisation includes the generation of a broad anticline deforming the Late Cretaceous strata (Fig. 13a–h). Faults surrounding the dome area offset Upper Triassic, Jurassic and Cretaceous strata. Conversely, faults are scarce in Lower Triassic and Permian strata imaged over the Palaeozoic evaporites (Figs. 5 and 6).

The coherence map at $Z = -980$ ms shows a circular geometry in map view, with a radial fault pattern limited to the Samson Dome (Fig. 8). This radial fault pattern reflects extension on the crest of the dome (Schultz-Ela, 1993; Withjack and Scheiner, 1982; Yin and Groshong, 2007). Similar radial fault patterns are found in many other geological structures resembling salt domes, such as igneous plutons and calderas (Acocella et al., 2004; Chadwick and Dieterich, 1995; Holohan et al., 2008; Walter and Troll, 2001); gneissic domes (Yin, 2004); mud volcanoes (Neurauter and Roberts, 1994) and mud diapirs (Hansen et al., 2005). On 3D seismic data the Samson Dome is markedly arched, with most faults offsetting the youngest Mesozoic horizons (Fig. 6). The Samson Dome, therefore, can be geometrically characterised as an open anticline. This type of structure favours buckling of the post-salt overburden forming broad structures with 4-way dip closures (Carter et al., 1982). The evolution of the Samson Dome comprises three distinct stages.

The first stage occurred during the Late Mesozoic (Fig. 13c–d). The growth of the Samson Dome resulted in the formation of an arched roof above Upper Palaeozoic evaporites, with associated radial faults and graben structures — including an apical block at the dome crests. The limits of the dome, as well as the radial faults, are indicated in Fig. 8. Faults crossing Upper Triassic to Upper Cretaceous strata follow the NW–SE trend of the Ottar Basin, whereas older Middle to Late Triassic (NE-trending) faults in the study area were formed early in the evolution of the Samson Dome and were reactivated later, as indicated by cross-cut relationships between faults and their corresponding throw-depth profiles (Fig. 10). In a second stage, the cessation of salt growth resulted in local dissolution of the dome (Fig. 13e–f). Dissolution was most likely initiated at the crest of the Samson Dome, evidenced by the lenticular geometry of the salt body (Figs. 5 and 6). The removal of the buried salt initiates and tends to be greater at the top and in more elevated parts of the diapir where the salt rises faster (cf. Ge and Jackson, 1998; Seni and Jackson, 1984). The third stage is associated with the collapse of the dome (Fig. 13g–h). Salt dissolution and loading imposed by post-salt overburden units is one of the main mechanisms to form collapse structures such as the one observed in the Samson Dome area (e.g., Clark et al., 1999; Ge and Jackson, 1998; Gutiérrez, 2004; McDonnell et al., 2007). Most faults in the study area are located on the Samson Dome and are underlain by Upper Palaeozoic evaporites, suggesting that these structures are related to salt removal and crestal collapse, with the uppermost Mesozoic layers being particularly affected by the development of Types B and C faults.

The model proposed here bears some similarity to data in Walter and Troll (2001) addressing the formation of volcanic calderas by doming and collapse (Fig. 13). Walter and Troll (2001) consider the inflation of volcanic chambers as capable of generating radial opening cracks that lead to their subsequent collapse - usually caused by later magma withdrawal from an underlying chamber. The collapse of calderas results in roof subsidence and closure of previously formed radial faults, and is accompanied by the formation of periphery en-echelon fractures with variable dips. Evidence for collapse of faults similar to those found on volcanic calderas are found in the interpreted seismic volume, where no substantial height differences are observed among tilted blocks at the crest of the Samson Dome. The greatest fault displacements occur for fault segments located close or above the salt dome (Fig. 9). As with volcanic calderas, dome collapse has resulted in maximum displacements of ~80 m in fault segments located on the crest of the Samson Dome. Displacement maxima tend to be of smaller magnitude in faults located distally from the dome. The rise and collapse of the anticlinal structure caused initially isolated segments to link, forming the radial fault pattern observed in the study area (Fig. 13).

Away from the Samson Dome, the seismic horizons seem to be flat and undisturbed by halokinesis. Nevertheless, the occurrence of Type C faults (Figs. 5 and 6) and small-scale fractures offsetting Cretaceous strata highlight the importance of the Late Cretaceous tectonics in the study area (Fig. 8). From key seismic lines and well 7224/7-1, it is clear that horizon H_7 is the only surface denoting significant erosion, being thinner at the top of the Samson Dome (Fig. 6). Away from the Samson Dome, thickness variations are not observed. These thickness variations are probably associated with Late Cretaceous-Paleogene erosion, which removed part of the Upper Cretaceous overburden that was uplifted and folded on top of the Samson Dome (Fig. 13).

8.2. Mechanism of fault linkage and reactivation

Displacement plots in Section 6.2 and 6.3 provide insights into the mode of propagation and linkage of faults around the Samson Dome. The observed fault geometries, and cross-cutting relationships, are also important clues to understand the evolution of the study area. For most representative Types A and B faults, throw-depth (T-z) data show maximum displacement close to horizon H_5 (Middle Triassic). Type A faults generally consist of either two or three segments and, in map view, radiate out from the Samson Dome (Fig. 8). The collapse of the salt dome is likely to have caused the individual fault segments to link, following a geometry akin to caldera-collapse structures, as discussed in Section 8.1 (Fig. 13). Lateral segmentation and linkage in Type A faults is presumably associated with the growth and collapse of the Samson Dome. For Type B faults, dome uplift is considered an important factor influencing their lateral and vertical propagation.

As for fault reactivation, the multiple displacement minima in F2 and F3 indicate that Type B faults consist of multiple overlapping fault segments (Figs. 9 and 10). For the majority of Type A and B faults, throw minima occur in Unit 3 (Late Jurassic) and in Unit 4 (Cretaceous). Reductions in fault throw observed for individual fault segments suggest reactivation along dip or dip linkage (Baudon and Cartwright, 2008b; Omosanya et al., 2015). We therefore propose that important fault reactivation took place in the Samson Dome area during the Cretaceous (e.g.

Faleide et al., 1993). A supporting evidence for reactivation in the Cretaceous is the generation of a third fault family, Type C, at this time.

8.3. Implications for petroleum systems in the Samson Dome and Ottar Basin

The interpreted seismic data provide little evidence for the presence of large-scale dim-spots. Vadakkepuliyambatta et al. (2013) considered the Samson Dome to form a large fluid-seepage structure based on the presence of an extensive area of dimmed strata on 2D seismic data. However the interpreted 3D seismic volume, which denotes a dramatic improvement in the quality of the seismic signal, does not image a dimmed zone. Our seismic cube makes it possible to delineate horizons and interpret faults with a great level of certainty, and bright reflections were only found at shallow depths above the Samson Dome. The largest bright spots are observed in Zone 2, which is located farther from the Samson Dome. Bright spots occur close to faults formed below horizons H_5 and H_7 in Zones 1 to 3, respectively. Some of these faults have their upper tips close to the seafloor (Figs. 8 and 12). A plausible argument is that the associated hydrocarbons or fluids migrated or leaked through the faults from deeper source rocks into shallow stratigraphic units.

The area where Zone 2 faults occur records a major erosional event at the transition between the Mesozoic to Cenozoic. We suggest that erosion of Upper Cretaceous strata in Unit 4 resulted in a reduction in the overburden stresses and, consequently, in migration and surface leakage of fluids towards the surface. This assumption is in agreement with previous data from other parts of the Barents Sea such as the Loppa High and Hammerfest Basin (Chand et al., 2008, 2012; Doré, 1995; Faleide et al., 1996; Ohm et al., 2008; Ostanin et al., 2012; Rajan et al., 2013). A similar fluid migration pattern is observed in the Loppa High, where shallow gas escapes to the water column through open faults (Chand et al., 2012). Fluid also migrates into shallow sediments and escapes at the seafloor through polygonal faults in the Hammerfest Basin (Ostanin et al., 2012), as shown by amplitude anomalies in the hanging-wall of the faults and shallow bright spots. It is important to notice, however, that evidence for sub-surface migration and fluid leakage in the Samson Dome area occurs only locally in the form of a few bright spots observed on the 3D seismic volume, and not through a large area as suggested by regional 2D data.

Leakage factor calculations indicate values ranging from 0.5 to 0.7 as the average for all the faults in the Zones 1 and 3, a character suggesting the likelihood of failure of seal units across the Samson Dome, and consequently a greater potential to leak fluids (Fig. 12). It must be noted that Zones 1 and 3 comprise large faults, offsetting horizons H_4 (Early Triassic) to H_7 (Late Cretaceous), but they also show small-scale faults within Unit 4. Fault F3 cuts a bright spot in section view, and could constitute a possible pathway for fluid migration in Zone 1 (Fig. 6). In Zone 3, bright spots in Unit 4 are intersected by Type-C faults, indicating the possibility of fluid migration to the surface. Zone 2, corresponding to the Samson Dome per se, shows NW-striking faults with higher leakage factors towards the surface, above the Late Cretaceous horizon (H_7). In contrast, they present relatively low leakage factors at depth.

Based on our results, we propose the lower leakage factor values at depth to relate to the geometry of collapse of this structure under its own weight. Despite consisting of multiple segments, faults in Zone 2 occur in a continuous plane, a character increasing the sealing capacity of these faults (Leveille et al., 1997). Considering that faults in Zone 2 show relatively larger values of slip tendency and lower leakage factors at depth relative to Zones 1 and 3, we propose that the stresses to which these faults are subjected at depth result in a tendency to 'lock' or close the faults, with subsequent generation of structural compartments capable of retaining fluids below the depth of Cretaceous-Jurassic strata.

An important implication of this work to the remainder of the Barents Sea is that the sealing capacity of faults on salt anticlines such as the Samson Dome increases with depth. Therefore, the trapping styles of hydrocarbons in salt structures across the Barents Sea exhibit greater variability than previously assumed. This is particularly noted in the largest branches of faults cross-cutting the Samson Dome, where stress analyses show leakage factor to be very high towards the surface, but decreasing significantly at depth below a neutral surface in which extension changes to compressional stresses at depth (e.g. Cosgrove and Ameen, 1999; Yeats, 1986) (Fig. 12). In such a setting, our Midland Valley Move® results not only provide evidence for decreasing leakage 'risk' with depth but also show that unravelling the evolution of structures such as the Samson Dome is key to understanding if Upper Palaeozoic strata are capable of accumulating economical volumes of hydrocarbons in the whole of the Barents and Arctic Seas.

9. Conclusions

The difficulty in dating halokinetic structures in the Barents Sea motivated the analysis of the Samson Dome as a case study applicable to other areas of the Arctic Sea, where salt tectonics exerts an important control on fault geometry and fluid flow. In parallel, this work aimed to evaluate the possibility of a late strike-slip reactivation affecting the Samson Dome area. However, no structural evidence to corroborate this event was found. This area was most likely subjected to extensional events, as revealed by paleostress analyses. The main conclusions of this work can be summarised as follows:

a) We divided the study area into three different zones with respect to the predominant strike of the faults. Type A faults are crestal faults that predominate in Zone 2; Type B are E-trending faults abundant to the northwest of the Samson Dome; Type C are small-scale faults generated at shallow levels around the Samson Dome.

b) Zone 1 is located to the north of the Samson Dome and comprises major E-trending and minor NW and NE-trending faults. Faults of types B and C predominate in Zone 1. Slip tendency values for these faults are relatively low but leakage factors are high, indicating a low sealing competence. A feature of interest is the occurrence of bright spots within Upper Triassic strata. These anomalies are intersected by Fault F3, which acted as a focused conduit for fluids in Zone 1.

c) Zone 2 is located over the Samson Dome. Acoustic anomalies in this zone are found below horizon H_5 (Middle Triassic) and between horizon H_7 (Late Cretaceous) and the seafloor. This zone is the most faulted, with Type A and C faults predominating with a prominent NW strike. Leakage factor values are higher towards the upper tip of faults. The leakage factor of faults decreases significantly with depth, indicating these faults may act as a barrier to fluids in clayey Triassic successions.

d) Zone 3 occurs to the south of the Samson Dome and is characterised by the occurrence of Type C faults, although in a smaller number than in Zones 1 and 2. The mean strike direction is NW and E. Reactivated NE–SW faults are also found in Zone 3. This zone shows small slip tendency values and a relatively high leakage factor. Acoustic anomalies around faults (bright spots) are found below horizon H_5 and near the seafloor.

e) The evolution of the Samson Dome as a salt anticline started during the Middle-Late Triassic, as recorded by deep-seated faults striking NE–SW at this same stratigraphic level. Pre-existing faults were reactivated during the Late Cretaceous, a period commonly regarded as reflecting tectonic quiescence in the Barents Sea. Locally, however, this was a tectonically active period associated with extension in the North Atlantic Ocean.

f) The study area was uplifted during a regional phase of Late Cretaceous extension; this event resulted in halokinesis in the Samson Dome region. Salt dissolution led to the collapse of the dome under its own weight.

g) Slip tendency and leakage factor analyses indicate the Samson Dome to be a smaller seepage structure than previously proposed. The variable stresses to which faults in the Samson Dome are subjected at depth result in a tendency to 'lock' and close the faults, with the

subsequent generation of structural compartments capable of retaining fluids below Jurassic and Cretaceous strata.

Acknowledgements

The authors would like to acknowledge the permission of Jonathan Turner and the BG Group, the NTNU-IPT database and NPD-Schlumberger for the use of the data included in this paper. This work was developed with the support of CAPES - Coordenaçao de Aperfeiçoamento de Pessoal de Nível Superior - Brasil. Schlumberger (providers of Petrel®), Midland Valley (Move®) and the Southwest Research Institute (3D Stress®) are acknowledged for the provision of the academic licences to Cardiff University 3D Seismic Lab. We thank editor J-P Avouac, J Cosgrove and an anonymous reviewer for their constructive comments.

References

Acocella, V., Funiciello, R., Marotta, E., Orsi, G., de Vita, S., 2004. The role of extensional structures on experimental calderas and resurgence. J. Volcanol. Geotherm. Res. 129, 199–217. http://dx.doi.org/10.1016/S0377-0273(03)00240-3.

Alves, T.M., Cartwright, J., Davies, R.J., 2009. Faulting of salt-withdrawal basins during early halokinesis: effects on the Paleogene Rio Doce Canyon system (Espírito Santo Basin, Brazil). Am. Assoc. Pet. Geol. Bull. 93, 617–652.

Alves, T.M., 2016. Polygonal mounds in the Barents Sea reveal sustained organic productivity towards the P-T boundary. Terra Nova 28, 50–59. http://dx.doi.org/10.1111/ter.12190.

Aydin, A., 2000. Fractures, faults, and hydrocarbon entrapment, migration and flow. Mar. Pet. Geol. 17, 797–814. http://dx.doi.org/10.1016/S0264-8172(00)00020-9.

Barnett, J.A., Mortimer, J., Rippon, J.H., Walsh, J.J., Watterson, J., 1987. Displacement geometry in the volume containing a single normal fault. Am. Assoc. Pet. Geol. Bull. 71, 925–937.

Barrère, C., Ebbing, J., Gernigon, L., 2009. Offshore prolongation of Caledonian structures and basement characterisation in the western Barents Sea from geophysical modelling. Tectonophysics 470, 71–88. http://dx.doi.org/10.1016/j.tecto.2008.07.012.

Baudon, C., Cartwright, J., 2008a. Early stage evolution of growth faults: 3D seismic insights from the Levant Basin, eastern Mediterranean. J. Struct. Geol. 30, 888–898. http://dx.doi.org/10.1016/j.jsg.2008.02.019.

Baudon, C., Cartwright, J., 2008b. The kinematics of reactivation of normal faults using high resolution throw mapping. J. Struct. Geol. 30, 1072–1084. http://dx.doi.org/10.1016/j.jsg.2008.04.008.

Biddle, K.T., 1985. Glossary—strike-slip deformation, basin formation, and sedimentation. In: Biddle, K.T., Christie-Blick, N. (Eds.), Strike-Slip Deformation. Basin Formation and Sedimentation. Special Publications of SEPM, Tulsa, pp. 375–386.

Breivik, A.J., Gudlaugsson, S.T., Faleide, J.I., 1995. Ottar Basin, Sw Barents Sea: a major Upper Palaeozoic rift basin containing large volumes of deeply buried salt. Basin Res. 7, 299–312. http://dx.doi.org/10.1111/j.1365-2117.1995.tb00119.x.

Breivik, A.J., Faleide, J.I., Gudlaugsson, S.T., 1998. Southwestern Barents Sea margin: late Mesozoic sedimentary basins and crustal extension. Tectonophysics 293, 21–44.

Breivik, A.J., Mjelde, R., Grogan, P., Shimamura, H., Murai, Y., Nishimura, Y., Kuwano, A., 2002. A possible Caledonide arm through the Barents Sea imaged by OBS data. Tectonophysics 355, 67–97.

Brown, A.R., 2011. Interpretation of Three-dimensional Seismic Data (American Association of Petroleum Geologists and the Society of Exploration Geophysicists).

Brudy, M., Kjørholt, H., 2001. Stress orientation on the Norwegian continental shelf derived from borehole failures observed in high-resolution borehole imaging logs. Tectonophysics 337, 65–84. http://dx.doi.org/10.1016/S0040-1951(00)00299-7.

Bugge, T., Elvebakk, G., Fanavoll, S., Mangerud, G., Smelror, M., Weiss, H.M., Gjelberg, J., Kristensen, S.E., Nilsen, K., 2002. Shallow stratigraphic drilling applied in hydrocarbon exploration of the Nordkapp Basin, Barents Sea. Mar. Pet. Geol. 19, 13–37.

Bungum, H., Alsaker, A., Kvamme, L.B., Hansen, R.A., 1991. Seismicity and seismotectonics of Norway and nearby continental shelf areas. J. Geophys. Res. http://dx.doi.org/10.1029/90JB02010.

Caine, J.S., Evans, J.P., Forster, C.B., 1996. Fault zone architecture and permeability structure. Geology 24, 1025–1028. http://dx.doi.org/10.1130/0091-7613(1996)024<1025.

Carruthers, D., Cartwright, J., Jackson, M.P.A., Schutjens, P., 2013. Origin and timing of layer-bound radial faulting around North Sea salt stocks: new insights into the evolving stress state around rising diapirs. Mar. Pet. Geol. 48, 130–148. http://dx.doi.org/10.1016/j.marpetgeo.2013.08.001.

Carter, N.L., Hansen, F.D., Senseny, P.E., 1982. Stress magnitudes in natural rock salt. J. Geophys. Res. Solid Earth 87, 9289–9300.

Cartwright, J.A., 1996. Polygonal Fault Systems: A New Type of Fault Structure Revealed by 3-D Seismic Data From the North Sea Basin.

Cartwright, J., Bouroullec, R., James, D., Johnson, H., 1998. Polycyclic motion history of some Gulf Coast growth faults from high-resolution displacement analysis. Geology 26, 819–822. http://dx.doi.org/10.1130/0091-7613(1998)026<0819:PMHOSG>2.3.CO;2.

Cartwright, J.A., Mansfield, C.S., 1998. Lateral displacement variation and lateral tip geometry of normal faults in the Canyonlands National Park, Utah. J. Struct. Geol. http://dx.doi.org/10.1016/S0191-8141(97)00079-5.

Chadwick, W.W., Dieterich, J.H., 1995. Mechanical modeling of circumferential and radial dike intrusion on Galapagos volcanoes. J. Volcanol. Geotherm. Res. 66, 37–52.

Chand, S., Mienert, J., Andreassen, K., Knies, J., Plassen, L., Fotland, B., 2008. Gas hydrate stability zone modelling in areas of salt tectonics and pockmarks of the Barents Sea suggests an active hydrocarbon venting system. Mar. Pet. Geol. 25, 625–636. http://dx.doi.org/10.1016/j.marpetgeo.2007.10.006.

Chand, S., Thorsnes, T., Rise, L., Brunstad, H., Stoddart, D., Bøe, R., Lågstad, P., Svolsbru, T., 2012. Multiple episodes of fluid flow in the SW Barents Sea (Loppa High) evidenced by gas flares, pockmarks and gas hydrate accumulation. Earth Planet. Sci. Lett. 331, 305–314.

Chapman, T.J., Williams, G.D., 1984. Displacement-distance methods in the analysis of fold-thrust structures and linked-fault systems. J. Geol. Soc. Lond. 141, 121–128.

Childs, C., Watterson, J., Walsh, J.J., 1995. Fault overlap zones within developing normal fault systems. J. Geol. Soc. Lond. http://dx.doi.org/10.1144/gsjgs.152.3.0535.

Childs, C., Walsh, J.J., Watterson, J., 1997. Complexity in fault zone structure and implications for fault seal prediction. Nor. Pet. Soc. Spec. Publ. 7, 61–72. http://dx.doi.org/10.1016/S0928-8937(97)80007-0.

Clark, J.A., Cartwright, J.A., Stewart, S.A., 1999. Mesozoic dissolution tectonics on the west central shelf, UK central North Sea. Mar. Pet. Geol. 16, 283–300.

Cocks, L.R.M., Torsvik, T.H., 2005. Baltica from the late Precambrian to mid-Palaeozoic times: the gain and loss of a terrane's identity. Earth-Sci. Rev. 72, 39–66.

Cosgrove, J.W., Ameen, M.S., 1999. A comparison of the geometry, spatial organization and fracture patterns associated with forced folds and buckle folds. Geol. Soc. Lond. Spec. Publ. 169, 7–21.

Dalland, A., Worsley, D., Ofstad, K., 1988. A lithostratigraphic scheme for the Mesozoic and Cenozoic succession offshore mid- and northern Norway. Norw. Petrol. Direct. Bull. 4, 87 No..

Dawers, N.H., Anders, M.H., 1995. Displacement-length scaling and fault linkage. J. Struct. Geol. 17. http://dx.doi.org/10.1016/0191-8141(94)00091-D.

Dengo, C.A., Røssland, K.G., 2013. Extensional tectonic history of the western Barents Sea. Struct. Tecton. Model. its Appl. to Pet. Geol. Nor. Pet. Soc. Spec. Publ. 1, 91–107.

Doré, A., 1991. The structural foundation and evolution of Mesozoic seaways between Europe and the Arctic. Palaeogeogr. Palaeoclimatol. Palaeoecol. 87, 441–492.

Doré, A., 1995. Barents Sea geology, petroleum resources and commercial potential. Arctic 48, 207–221.

Ehrenberg, S.N., Nielsen, E., Svånå, T.A., Stemmerik, L., 1998. Depositional evolution of the Finnmark carbonate platform, Barents Sea: results from wells 7128/6-1 and 7128/4-1. Nor. Geol. Tidsskr. 78, 185–224.

Elvebakk, G., Hunt, D.W., Stemmerik, L., 2002. From isolated buildups to buildup mosaics: 3D seismic sheds new light on Upper Carboniferous–Permian fault controlled carbonate buildups, Norwegian Barents Sea. Sediment. Geol. 152, 7–17.

Faleide, J.I., Gudlaugsson, S.T., Jacquart, G., 1984. Evolution of the western Barents Sea. Mar. Pet. Geol. http://dx.doi.org/10.1016/0264-8172(84)90082-5.

Faleide, J.I., Vågnes, E., Gudlaugsson, S.T., 1993. Late Mesozoic–Cenozoic evolution of the south-western Barents Sea in a regional rift-shear tectonic setting. Mar. Pet. Geol. 10, 186–214. http://dx.doi.org/10.1016/0264-8172(93)90104-Z.

Faleide, J.I., Solheim, A., Fiedler, A., Hjelstuen, B.O., Andersen, E.S., Vanneste, K., 1996. Late Cenozoic evolution of the western Barents Sea–Svalbard continental margin. Glob. Planet. Chang. http://dx.doi.org/10.1016/0921-8181(95)00012-7.

Faleide, J.I., Tsikalas, F., Breivik, A.J., Mjelde, R., Ritzmann, O., Engen, O., Wilson, J., Eldholm, O., 2008. Structure and evolution of the continental margin off Norway and the Barents Sea. Episodes 31, 82–91. http://dx.doi.org/10.1016/j.strusafe.2006.11.005.

Fejerskov, M., Lindholm, C., Myrvang, A., Bungum, H., 2000. Crustal stress in and around Norway: a compliation of in situ stress observations. Geol. Soc. Lond. Spec. Publ. 167, 441–449. http://dx.doi.org/10.1144/GSL.SP.2000.167.01.18.

Gabrielsen, R., 1984. Long-lived fault zones and their influence on the tectonic development of the southwestern Barents Sea. J. Geol. Soc. Lond.

Gabrielsen, R.H., Faerseth, R.B., Jensen, L.N., Kalheim, J.E., Riis, F., 1990. Structural elements of the Norwegian continental shelf part I: the Barents Sea region. Nor. Pet. Dir. Bull. 6, 45 No..

Gamboa, D., Alves, T., Cartwright, J., Terrinha, P., 2010. MTD distribution on a 'passive' continental margin: the Espírito Santo Basin (SE Brazil) during the Palaeogene. Mar. Pet. Geol. 27, 1311–1324. http://dx.doi.org/10.1016/j.marpetgeo.2010.05.008.

Ge, H., Jackson, M.P., 1998. Physical modeling of structures formed by salt withdrawal: implications for deformation caused by salt dissolution. Am. Assoc. Pet. Geol. Bull. 82, 228–250.

Gee, D., Fossen, H., Henriksen, N., Higgins, A., 2008. From the early Paleozoic platforms of Baltica and Laurentia to the Caledonide Orogen of Scandinavia and Greenland. Episodes 31, 44–51.

Gernigon, L., Brönner, M., 2012. Late Palaeozoic architecture and evolution of the south-western Barents Sea: insights from a new generation of aeromagnetic data. J. Geol. Soc. Lond. 169, 449–459.

Gernigon, L., Brönner, M., Roberts, D., Olesen, O., Nasuti, A., Yamasaki, T., 2014. Crustal and basin evolution of the southwestern Barents Sea: from Caledonian orogeny to continental breakup. Tectonics 33, 347–373. http://dx.doi.org/10.1002/2013TC003439.

Glørstad-Clark, E., Faleide, J.I., Lundschien, B.A., Nystuen, J.P., 2010. Triassic seismic sequence stratigraphy and paleogeography of the western Barents Sea area. Mar. Pet. Geol. 27, 1448–1475. http://dx.doi.org/10.1016/j.marpetgeo.2010.02.008.

Gölke, M., Brudy, M., 1996. Orientation of crustal stresses in the North Sea and Barents Sea inferred from borehole breakouts. Tectonophysics 266, 25–32. http://dx.doi.org/10.1016/S0040-1951(96)00181-3.

Gölke, M., Coblentz, D., 1996. Origins of the European regional stress field. Tectonophysics 266, 11–24. http://dx.doi.org/10.1016/S0040-1951(96)00180-1.

Gudlaugsson, S.T., Faleide, J.I., Johansen, S.E., Breivik, A.J., 1998. Late Palaeozoic structural development of the south-western Barents Sea. Mar. Pet. Geol. http://dx.doi.org/10.1016/S0264-8172(97)00048-2.

Gutiérrez, F., 2004. Origin of the salt valleys in the Canyonlands section of the Colorado plateau: evaporite-dissolution collapse versus tectonic subsidence. Geomorphology 57, 423–435.
Hansen, J.P.V., Cartwright, J.A., Huuse, M., Clausen, O.R., 2005. 3D seismic expression of fluid migration and mud remobilization on the Gjallar ridge, offshore mid-Norway. Basin Res. 17, 123–139.
Heidbach, O., Tingay, M., Barth, A., Reinecker, J., Kurfeß, D., Müller, B., 2008. The World Stress Map Database Release. p. 2008 http://dx.doi.org/10.1594/GFZ.WSM.Rel2008.
Henriksen, E., Bjornseth, H.M., Hals, T.K., Heide, T., Kiryukhina, T., Klovjan, O.S., Larssen, G.B., Ryseth, A.E., Ronning, K., Sollid, K., Stoupakova, A., 2011a. Uplift and Erosion of the Greater Barents Sea: Impact on Prospectivity and Petroleum Systems. Geol. Soc, London, Mem http://dx.doi.org/10.1144/M35.17.
Henriksen, E., Ryseth, A.E., Larssen, G.B., Heide, T., Ronning, K., Sollid, K., Stoupakova, A.V., 2011b. Tectonostratigraphy of the Greater Barents Sea: Implications for Petroleum Systems. Geol. Soc, London, Mem http://dx.doi.org/10.1144/M35.10.
Holohan, E.P., De Vries, B.V.W., Troll, V.R., 2008. Analogue models of caldera collapse in strike-slip tectonic regimes. Bull. Volcanol. 70, 773–796.
Hudec, M.R., Jackson, M.P.A., 2007. Terra infirma: understanding salt tectonics. Earth-Sci. Rev. 82, 1–28. http://dx.doi.org/10.1016/j.earscirev.2007.01.001.
Jensen, L.N., Sørensen, K., 1992. Tectonic framework and halokinesis of the Nordkapp Basin, Barents Sea. Struct. Tecton. Model. its Appl. to Pet. Geol. Nor. Pet. Soc. Spec. Publ. 1, 109–120.
Johansen, S.E., Ostisty, B.K., Birkeland, ø., Fedorovsky, Y.F., Martirosjan, V.N., Christensen, O.B., Cheredeev, S.I., Ignatenko, E.A., Margulis, L.S., 1993. Hydrocarbon potential in the Barents Sea region: play distribution and potential. Norwegian Petroleum Society Special Publications, pp. 273–320 http://dx.doi.org/10.1016/B978-0-444-88943-0.50024-1.
Jolley, S.J., Fisher, Q.J., Ainsworth, R.B., 2010. Reservoir compartmentalization: an introduction. Geol. Soc. Lond. Spec. Publ. 347, 1–8. http://dx.doi.org/10.1144/SP347.1.
Klausen, T.G., Mørk, A., 2014. The Upper Triassic paralic deposits of the De Geerdalen formation on Hopen: outcrop analog to the subsurface Snadd formation in the Barents Sea. Am. Assoc. Pet. Geol. Bull. 98, 1911–1941.
Klausen, T.G., Ryseth, A.E., Helland-Hansen, W., Gawthorpe, R., Laursen, I., 2015. Regional development and sequence stratigraphy of the Middle to Late Triassic Snadd formation, Norwegian Barents Sea. Mar. Pet. Geol. 62, 102–122.
Klein, R.J., Barr, M.V., 1986. Regional state of stress in western Europe. In: Stephenson, O. (Ed.), Rock Stress and Rock Stress Measurement. Centrek Publ, Stockholm, pp. 33–44.
Knipe, R.J., 1997. Juxtaposition and seal diagrams to help analyze fault seals in hydrocarbon reservoirs. Am. Assoc. Pet. Geol. Bull. 81, 187–195. http://dx.doi.org/10.1306/522B42DF-1727-11D7-8645000102C1865D.
Knipe, R.J., Jones, G., Fisher, Q.J., 1998. Faulting, fault sealing and fluid flow in hydrocarbon reservoirs: an introduction. Geol. Soc. Lond. Spec. Publ. http://dx.doi.org/10.1144/GSL.SP.1998.147.01.01.
Koyi, H., Talbot, C.J., Tørudbakken, B.O., 1993. Salt diapirs of the southwest Nordkapp Basin: analogue modelling. Tectonophysics 228, 167–187.
Larssen, G.B., Elvebakk, G., Henriksen, L.B., Nilsson, I., Samuelsberg, T.J., Stemmerik, L., Worsley, D., Kristensen, S.E., Svånå, T.A., 2002. Upper Palaeozoic lithostratigraphy of the Southern Norwegian Barents Sea. Norw. Petrol. Direct. Bull. 9, 76.
Leveille, G.P., Knipe, R., More, C., Ellis, D., Dudley, G., Jones, G., Fisher, Q.J., Allinson, G., 1997. Compartmentalization of Rotliegendes gas reservoirs by sealing faults, Jupiter fields area, southern North Sea. Geol. Soc. London, Spec. Publ. 123, 87–104. http://dx.doi.org/10.1144/GSL.SP.1997.123.01.06.
Lindholm, C.D., Bungum, J., Bratli, R.K., Aadnøy, B.S., Dahl, N., Tørudbakken, B., Atakan, K., 1995. Crustal stress in the northern North Sea as inferred from borehole breakouts and earthquake focal mechanisms. Terra Nova 7, 51–59. http://dx.doi.org/10.1111/j.1365-3121.1995.tb00667.x.
Lindholm, C.D., Bungum, H., Hicks, E., Villagran, M., 2000. Crustal stress and tectonics in Norwegian regions determined from earthquake focal mechanisms. Geol. Soc. London, Spec. Publ. 167, 429–439. http://dx.doi.org/10.1144/GSL.SP.2000.167.01.17.
Lonergan, L., Cartwright, J., Jolly, R., 1998. The geometry of polygonal fault systems in tertiary mudrocks of the North Sea. J. Struct. Geol. 20, 529–548. http://dx.doi.org/10.1016/S0191-8141(97)00113-2.
Mansfield, C.S., Cartwright, J.A., 1996. High resolution fault displacement mapping from three-dimensional seismic data: evidence for dip linkage during fault growth. J. Struct. Geol. 18, 249–263. http://dx.doi.org/10.1016/S0191-8141(96)80048-4.
McDonnell, A., Loucks, R.G., Dooley, T., 2007. Quantifying the origin and geometry of circular sag structures in northern Fort Worth Basin, Texas: Paleocave collapse, pull-apart fault systems, or hydrothermal alteration? Am. Assoc. Pet. Geol. Bull. 91, 1295–1318.
McFarland, J.M., Morris, A.P., Ferrill, D.A., 2012. Stress inversion using slip tendency. Comput. Geosci. 41, 40–46.
Valley, M., 2014. Midland Valley Move Application.
Mørk, A., Elvebakk, G., 1999. Lithological description of subcropping lower and middle Triassic Rocks from the Svalis Dome, Barents Sea. Polar Res. 18, 83–104. http://dx.doi.org/10.1111/j.1751-8369.1999.tb00278.x.
Morris, A., Ferrill, D.A., Henderson, D.B., 1996. Slip-tendency analysis and fault reactivation. Geology 24, 275–278. http://dx.doi.org/10.1130/0091-7613(1996)024<0275.
Müller, B., Zoback, M.L., Fuchs, K., Mastin, L., Gregersen, S., Pavoni, N., Stephansson, O., Ljunggren, C., 1992. Regional patterns of tectonic stress in Europe. J. Geophys. Res. http://dx.doi.org/10.1029/91JB01096.
Muraoka, H., Kamata, H., 1983. Displacement distribution along minor fault traces. J. Struct. Geol. 5, 483–495. http://dx.doi.org/10.1016/0191-8141(83)90054-8.
Neurauter, T.W., Roberts, H.H., 1994. Three generations of mud volcanoes on the Louisiana continental slope. Geo-Mar. Lett. 14, 120–125.
Nicol, A., Watterson, J., Walsh, J.J., Childs, C., 1996. The shapes, major axis orientations and displacement patterns of fault surfaces. J. Struct. Geol. http://dx.doi.org/10.1016/S0191-8141(96)80047-2.
Nicol, A., Gillespie, P.A., Childs, C., Walsh, J.J., 2002. Relay zones between mesoscopic thrust faults in layered sedimentary sequences. J. Struct. Geol. 24, 709–727.
Nilsen, K.T., Henriksen, E., Larsen, G.B., 1993. Exploration of the Late Palaeozoic carbonates in the southern Barents Sea—a seismic stratigraphic study. Arct. Geol. Pet. Potential, Norw. Pet. Soc. Spec. Publ 2, 393–404.
Nilsen, K.T., Vendeville, B.C., Johansen, J.-T., 1995. Influence of Regional Tectonics on Halokinesis in the Nordkapp Basin, Barents Sea.
Nøttvedt, A., Cecchi, M., Gjelberg, J.G., Kristensen, S.E., Lønøy, A., Rasmussen, A., Rasmussen, E., Skott, P.H., van Veen, P.M., 1993. Svalbard-Barents sea correlation: a short review. Norwegian Petroleum Society Special Publications, pp. 363–375 http://dx.doi.org/10.1016/B978-0-444-88943-0.50027-7.
Ohm, S.E., Karlsen, D.A., Austin, T.J.F., 2008. Geochemically driven exploration models in uplifted areas: examples from the Norwegian Barents Sea. Am. Assoc. Pet. Geol. Bull. 92, 1191–1223.
Omosanya, K.O., Alves, T.M., 2014. Mass-transport deposits controlling fault propagation, reactivation and structural decoupling on continental margins (Espírito Santo Basin, SE Brazil). Tectonophysics 628, 158–171. http://dx.doi.org/10.1016/j.tecto.2014.04.045.
Omosanya, K.O., Johansen, S.E., Harishidayat, D., 2015. Evolution and Character of Supra-Salt Faults in the Easternmost Hammerfest Basin, SW Barents Sea. Mar. Pet, Geol.
Ostanin, I., Anka, Z., Di Primio, R., Bernal, A., 2012. Hydrocarbon Leakage Above the Snøhvit Gas Field, Hammerfest Basin SW Barents Sea. First Break. 30.
Peacock, D.C.P., 1991. A comparison between the displacement geometries of veins and normal faults at Kilve, Somerset. Geoscience in South-West England, pp. 363–367.
Peacock, D.C.P., Sanderson, D., 1991. Displacements, segment linkage and relay ramps in normal fault zones. J. Struct. Geol. 13, 721–733. http://dx.doi.org/10.1016/0191-8141(91)90033-F.
Perez-Garcia, C., Safronova, P.A., Mienert, J., Berndt, C., Andreassen, K., 2013. Extensional rise and fall of a salt diapir in the Sørvestsnaget Basin, SW Barents Sea. Mar. Pet. Geol. 46, 129–143. http://dx.doi.org/10.1016/j.marpetgeo.2013.05.010.
Pollard, D.D., Segall, P., 1987. Theoretical displacements and stresses near fractures in rock: with applications to faults, joints, veins, dikes, and solution surfaces. Fract. Mech. rock 277, 277–349.
Rajan, A., Bünz, S., Mienert, J., Smith, A.J., 2013. Gas hydrate systems in petroleum provinces of the SW-Barents Sea. Mar. Pet. Geol. 46, 92–106. http://dx.doi.org/10.1016/j.marpetgeo.2013.06.009.
Ranalli, G., Chandler, T.E., 1975. The stress field in the upper crust as determined from in situ measurements. Geol. Rundsch. 64, 653–674. http://dx.doi.org/10.1007/BF01820688.
Ritzmann, O., Faleide, J.I., 2007. Caledonian basement of the western Barents Sea. Tectonics 26. http://dx.doi.org/10.1029/2006TC002059.
Roberts, D., 2003. The Scandinavian Caledonides: event chronology, palaeogeographic settings and likely modern analogues. Tectonophysics 365, 283–299. http://dx.doi.org/10.1016/S0040-1951(03)00026-X.
Ryseth, A., Augustson, J.H., Charnock, M., Haugerud, O., Knutsen, S.M., Midbøe, P.S., Sundsbø, G., 2003. Cenozoic stratigraphy and evolution of the Sørvestsnaget Basin, southwestern Barents Sea. Norwegian Journal of Geology/Norsk Geologisk Forening 83 (2).
Safronova, P.A., Henriksen, S., Andreassen, K., Laberg, J.S., Vorren, T.O., 2014. Evolution of shelf-margin clinoforms and deep-water fans during the middle Eocene in the Sorvestsnaget Basin, southwest Barents Sea. Am. Assoc. Pet. Geol. Bull. 98, 515–544.
Schultz-Ela, D.D., Jackson, M.P. a., Vendeville, B.C., 1993. Mechanics of active salt diapirism. Tectonophysics 228, 275–312. doi:http://dx.doi.org/10.1016/0040-1951(93)90345-K
Seni, S.J., Jackson, M.P.A., 1984. Sedimentary Record of Cretaceous and Tertiary Salt Movement, East Texas Basin: Times, Rates, and Volumes of Salt Flow and Their Implications for Nuclear Waste Isolation and Petroleum Exploration. Bureau of Economic Geology, University of Texas of Austin.
Smelror, M., 1994. Jurassic stratigraphy of the Western Barents sea region: a review. Geobios 27, 441–451. http://dx.doi.org/10.1016/S0016-6995(94)80165-7.
Smelror, M., Petrov, O.V., Larssen, G.B., Werner, S.C., 2009. Geological history of the Barents Sea. Nor. Geol. Unders. 1–135.
Smith, L., Forster, C.B., Evans, J.P., 1990. Interaction between Fault Zones, Fluid Flow and Heat Transfer at the Basin Scale.
Soper, N.J., Strachan, R.A., Holdsworth, R.E., Gayer, R.A., Greiling, R.O., 1992. Sinistral transpression and the Silurian closure of Iapetus. J. Geol. Soc. Lond. 149, 871–880.
Stemmerik, L., 2000. Late Palaeozoic evolution of the North Atlantic margin of Pangea. Palaeogeogr. Palaeoclimatol. Palaeoecol. 161, 95–126.
Stephansson, O., 1993. Rock stress in the Fennoscandian shield. Comprehensive Rock Engineering, first ed. Pergamon Press, Oxford.
Stewart, S.A., 2006. Implications of passive salt diapir kinematics for reservoir segmentation by radial and concentric faults. Mar. Pet. Geol. 23, 843–853. http://dx.doi.org/10.1016/j.marpetgeo.2006.04.001.
Stoupakova, A.V., Henriksen, E., Burlin, Y.K., Larsen, G.B., Milne, J.K., Kiryukhina, T.A., Golynchik, P.O., Bordunov, S.I., Ogarkova, M.P., Suslova, A.A., 2011. The Geological Evolution and Hydrocarbon Potential of the Barents and Kara Shelves. Geol. Soc, London, Mem http://dx.doi.org/10.1144/M35.21.
Talbot, C., Rönnlund, P., Schmeling, H., 1991. Diapiric spoke patterns. Tectonophysics 188, 187–201.
Torsvik, T., Smethurst, M., Meert, J., Vandervoo, R., Mckerrow, W., Brasier, M., Sturt, B., Walderhaug, H., 1996. Continental break-up and collision in the Neoproterozoic and Palaeozoic — a tale of Baltica and Laurentia. Earth-Sci. Rev. 40, 229–258. http://dx.doi.org/10.1016/0012-8252(96)00008-6.

Vadakkepuliyambatta, S., Bünz, S., Mienert, J., Chand, S., 2013. Distribution of subsurface fluid-flow systems in the SW Barents Sea. Mar. Pet. Geol. 43, 208–221.
Vendeville, B.C., Jackson, M.P.A., 1992. The rise of diapirs during thin-skinned extension. Mar. Pet. Geol. 9, 331–354. http://dx.doi.org/10.1016/0264-8172(92)90047-I.
Vendeville, B.C., 2002. A New Interpretation of Trusheim's Classic Model of Salt-Diapir Growth.
Vorren, T.O., Richardsen, G., Knutsen, S.-M., Henriksen, E., 1991. Cenozoic erosion and sedimentation in the western Barents Sea. Mar. Pet. Geol. http://dx.doi.org/10.1016/0264-8172(91)90086-G.
Walsh, J.J., Watterson, J., 1987. Distributions of cumulative displacement and seismic slip on a single normal fault surface. J. Struct. Geol. 9, 1039–1046.
Walsh, J.J., Watterson, J., Heath, A.E., Childs, C., 1998. Representation and scaling of faults in fluid flow models. Pet. Geosci. http://dx.doi.org/10.1144/petgeo.4.3.241.
Walsh, J.J., Bailey, W.R., Childs, C., Nicol, A., Bonson, C.G., 2003. Formation of segmented normal faults: a 3-D perspective. J. Struct. Geol. 25, 1251–1262.
Walter, T.R., Troll, V.R., 2001. Formation of caldera periphery faults: an experimental study. Bull. Volcanol. 63, 191–203.
Withjack, M., Scheiner, C., 1982. Fault patterns associated with domes — an experimental and analytical study. Am. Assoc. Pet. Geol. Bull. 66, 302–316.
Worsley, D., 2008. The post-Caledonian development of Svalbard and the western Barents Sea. Polar Res. 298–317 http://dx.doi.org/10.1111/j.1751-8369.2008.00085.x.
Yeats, R.S., 1986. Faults related to folding with examples from New Zealand. R. Soc. New Zeal. Bull. 24, 273–292.
Yin, A., 2004. Gneiss domes and gneiss dome systems. Geol. Soc. Am. Spec. Pap. 380, 1–14.
Yin, H., Groshong, R.H., 2007. A three-dimensional kinematic model for the deformation above an active diapir. Am. Assoc. Pet. Geol. Bull. 91, 343–363. http://dx.doi.org/10.1306/10240606034.
Zoback, M.D., 2010. Reservoir Geomechanics. Cambridge University Press.